ALTAIR

AIAA Undergraduate Engine Design Competition

Final Proposal - May 2017

Team Leader

Badriveer Thota

Team Members

Neelesh Katoch

Dhruv Vijapuri

Naman Soni

Anushka Vargantwar

Nitin Ramseshan

Keshu Jat

Faculty Advisor

Prof. Bibin John

Declaration

Badriveer Thota
#808649

Neelesh Katoch
#819250

Dhruv Vijapuri
#819129

Naman Soni
#819127

Anushka Vargantwar
#819246

Nitin Ramaseshan
#819125

Keshu Jat
#819213

Abstract

ALTAIR is a candidate engine for next generation single engine turboprop aircraft designed to replace the current front runner PT6A-68B used in the Pilatus PC-21 and is expected to enter service by the year 2025.

ALTAIR is lighter by 12.6%, has an improved fuel burn of more than 20% and a 25% greater power output as compared to the specified baseline engine whilst being economically similar and adhering to the present technological developments making it both efficient and realistic.

The engine uses a 4-stage axial compressor and single-stage centrifugal compressor in its compressor section, a reverse-flow annular combustor and a single-stage high pressure turbine and two-stage low pressure turbine in its turbine section which is similar to the baseline engine. ALTAIR is capable of cruising at 10000ft with a range of 1570NM.

Acknowledgements

We would like to first extend our gratitude to VIT University administration especially to the Honourable Chancellor, Pro Vice Chancellor and the Director of Students' Welfare for the successful completion of this project. We would also like to thank SEDS India Permanent Trustee- Prof. Geetha Manivasagam and our SEDS-VIT Faculty Coordinator- Prof. Vijaya Kumar Manupati and Prof. Nageswara Rao Muktinutalapati for their unflinching faith and guidance. We thank our Faculty Coordinator Prof. Bibin John for his constant supervision throughout our journey and the SEDS-VIT Projects committee for providing us the platform to accomplish this endeavor satisfactorily.

We also thank the competition organizers and SoftInWay for their prompt and immediate responses to all our queries.

Our special thanks to the SEDS-VIT CanSat'17 team for their relentless and invaluable efforts to support our undertaking.

Table of Contents

List of Figures

List of Tables

1. Introduction

AIAA Undergraduate Engine Design Competition 2016-17 Request for Proposal (RFP) gives the guidelines to design Candidate Engines for a Next Generation Single-Engine Turboprop Aircraft to replace the current engine in the Pilatus PC-21 aircraft by the year 2025 [1]. This report presents the preliminary design of ALTAIR engine which offers enhanced fuel burn, longer range and greater power whilst satisfying the thrust requirements as stated in Table 1 as per RFP.

Table 1: *In-Flight Thrust Requirements [1]*

General Thrust Requirements (Total for 1 engine)		
Takeoff	Sea Level Static+ 27F Std. Day	1,600 shp
Cruise	337 KTAS, 10,000	1,300 shp

GasTurb 12 was used to determine the optimum engine cycle and the corresponding cycle summary was used to determine the aerothermodynamics of the engine's turbomachinery in AxStream.

1.1 ALTAIR Summary

The following Compliance Matrix (Table 2), Engine Summary Data (Table 3) and Flow Station Data (Table 4) are obtained for ALTAIR engine and the process is outlined in Cycle Analysis.

Table 2: *Compliance Matrix*

Performance	
Maximum Speed	370 KEAS
Cruise Speed	337 KTAS at 10,000 feet
Mission Fuel Burn	756 lbm
Cruise ESFC	0.37395 lb/shp/h
Takeoff ESFC	0.41702 lb/shp/h
Engine Weight	500 lbs
Engine Diameter	17”
Required Trade Studies	
Engine Cycle Design Space Carpet Plots	Page 11, 12, 13
In-Depth Cycle Summary	Page 3
Final engine flow path	Page 8
Final cycle study using chosen cycle program	Page 14
Detailed stage-by-stage turbomachinery design information	C: Page 21; T: Page 38
Detailed design of velocity triangles	C: Page 27-30; T: Page 40-44

***Table 3:** Engine Summary*

Summary Data	
Design MN	0 (SLS)
Design Altitude	0 (SLS)
Design Fan Mass Flow	10.58 lbm/s
Design Shaft Horsepower	1648.48 shp
Design ESFC	0.41702 lb/shp/h
Design Overall Pressure Ratio	11.6
Design T4.1	2458.23 ºR
Design Engine Pressure Ratio	11.6
Design LPC Pressure Ratio	3.786
Design Chargeable Cooling Flow	0
Design Non-Chargeable Cooling Flow	0
Design Adiabatic Efficiency for Each Turbine	0.912
Design Polytropic Efficiency for Each Compressor	0.9
Design Shaft Power Loss	1%
Design Gas Generator Shaft RPM	36830.3
Design Free/Power Turbine Shaft RPM	30000
Additional Information	
Design HP/LP Shaft Off-Take Power	50 hp
Design Customer Bleed Flow	7%

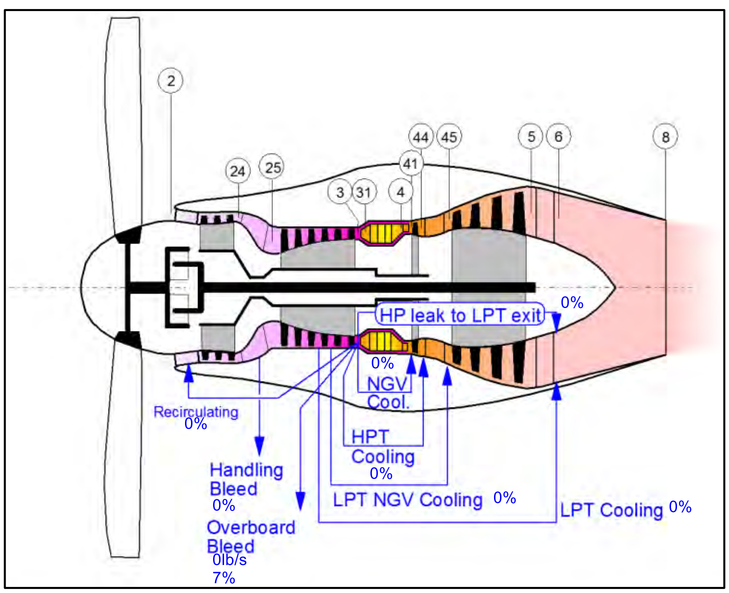

***Figure 1:** Engine stations with their location [2]*

Table 4: *Flow Station Data obtained from GasTurb12*

	Units	St 2	St 24	St 25	St 3	St 4	St 44	St 45	St 5	St 6	St 8
Mass Flow	lb/s	10.58	10.58	10.58	10.58	10.0486	10.0486	10.0486	10.0486	10.0486	10.0486
Total Temperature	R	518.67	789.614	789.614	1115.07	2458.23	1929.79	1929.79	1514.44	1514.44	1514.44
Static Temperature	R	493.933	752.746	752.746	1106.85	2443.48	1855.86	1855.86	1453.41	1493.52	1468.75
Total Pressure	psia	14.696	55.6457	55.6457	170.448	159.369	50.9225	50.6679	16.9453	16.6064	16.6064
Static Pressure	psia	12.3885	46.9437	46.9437	165.846	155.284	43.3127	43.0961	14.3807	15.71	14.6959
Velocity	ft/s	544.799	670.96	670.96	323.144	467.436	1025.55	1025.55	914.125	535.186	790.939
Area	in²	41.3093	13.4899	13.4899	11.658	18.0474	22.3987	22.5113	59.2727	95.2322	67.7423
Mach Number		0.5	0.5	0.5	0.2	0.2	0.5	0.5	0.5	0.289	0.430485
Density	lb/ft³	0.067696	0.168322	0.168322	0.404416	0.171528	0.062992	0.062678	0.026706	0.028391	0.027006
Fuel-Air-Ratio		0	0	0	0	0.021267	0.021267	0.021267	0.021267	0.021267	0.021267

1.2 Comparison between different turboprops

Modern operational turboprop engines have been listed below. The design of ALTAIR is based on the following trade-off studies performed. Some of the desired characteristics in gas turbine engines are:

- Extension in time between engine overhauls
- Commercial narrow-body jets
- Reduced overall engine size and weight
- Operation at higher temperatures with much better maintenance intervals
- Better pressure ratio with less mass flow rate
- Better thrust-to-weight ratio

Table 5: *Comparison between Small Turboprop Engines*

Engine	Rolls Royce Dart 528 [3]	General Electric CT7 [7]	Pratt & Whitney PW118 [4, 5]	Allison T56/501D Series III [3]
Aircraft	Boeing B-17F Flying Fortress	CASA/IPTN CN-235	Embraer 120	Lockheed L-100
Centrifugal Compressor	2	1	2	0
Turbine	3	4	4	4
Power (shp)	1825	2043	1800	5000
Engine RPM	15000	22000	1313	13820
Weight (lb)	1415	400	861	1835
TSFC (lbm/hr/lbf)	0.57	0.433	NA	NA
Axial Compressor	0	5	0	14
OPR	5.62:1	17:01	18:1	9.5:1
Length (in)	98	47	81	146.1
Diameter (in)	45	25 or 26	25	27
Mass flow rate (lb/sec)	23.5	NA	NA	32.35

Table 6: *Comparison between Large Turboprop Engines*

Engine	PT6A [1]	Garret TPE331 [8]	Allison Model 250 [3]
Aircraft	Pilatus PC-21	Pilatus/Fairchild PC-6C Turbo-Porter	Aermacchi M-290 RediGO
Centrifugal Compressor	1	2	1
Turbine	2	3	4
Power (shp)	1250	575	250
Engine RPM	30000	1591	2030
Weight (lb)	572	336	136
TSFC (lbm/hr/lbf)	0.566	0.49	0.77
Axial Compressor	4	0	6
OPR	9.45:1	10.55:1	6.2:1
Length (in)	71.3	46	40.5
Diameter (in)	19	21	22.5
Mass flow rate (lb/sec)	10.6	7.7	3

Conclusion

- It is observed that the primary effort is directed towards driving the propeller. One such method of doing this is by using the free turbine. So, in ALTAIR, one free turbine is incorporated.
- Further by this comparison it was also found that the power output and overall pressure ratios are more for those engines with Reverse Annular flow having approximately the same power output with improved power to weight ratio.

2. Constraint Analysis

Constraint analysis solves the major purpose of determining the thrust loading and wing loading for the various segments of the aircraft's flight. In order to find the solution space for the aircraft, a plot of thrust loading versus wing loading is made for various segments. The constraint analysis is carried out using the procedure described in [9].

Based on the data given in Table 7 [1], we obtain the aspect ratio using the equation

$$AR = \frac{b^2}{S} = 5.298$$

Using the obtained aspect ratio value, we determine Oswald's coefficient 'e'

$$e = 1.78(1 - 0.045 * (AR)^{0.68}) - 0.64 = 0.891$$

Table 7: *Some General Characteristics of the Next Single-Engine Turboprop Aircraft [1]*

General Characteristics	
Crew	2
Length	36.91ft
Wing Span	29.91 ft
Height	12.33 ft
Wing Area	168.85 ft^2
Max Take-off Weight	6,824 lbm
Power plant	1 x turboshaft engine; 1600 shp @ SLS
Performance	
Maximum Speed	370KEAS
Cruise Speed	337KTAS at 10,000 ft
Range	720NM
Service Ceiling	38,000 ft

Using the above two obtained values we obtain the lift induced drag constant 'k'.

$$k = \frac{1}{(AR)\pi e} = 0.067$$

Using the equations described below, an iterative operation was conducted in Excel to obtain optimum values of (T/W) and (W/S).

Take-off: $$\frac{T}{W} = \frac{V_{LOF}^2}{2gS_G} + \frac{qC_D}{\frac{W}{S}} + \mu\left(1 - \frac{qC_L}{\frac{W}{S}}\right)$$

Cruise: $$\frac{T}{W} = qC_{Dmin}\left(\frac{1}{W/_S}\right) + k\left(\frac{1}{q}\right)\left(\frac{W}{S}\right)$$

Service Ceiling: $$\frac{T}{W} = \frac{V_V}{\sqrt{\frac{2}{\rho}(\frac{W}{S})\sqrt{\frac{k}{3\,C_{Dmin}}}}} + 4\sqrt{\frac{kC_{Dmin}}{3}}$$

Landing: $$\frac{W}{S} = \frac{\frac{1}{2}(\rho V_{SL}^2 C_{Lmax})}{\frac{W_L}{W_{TO}}}$$

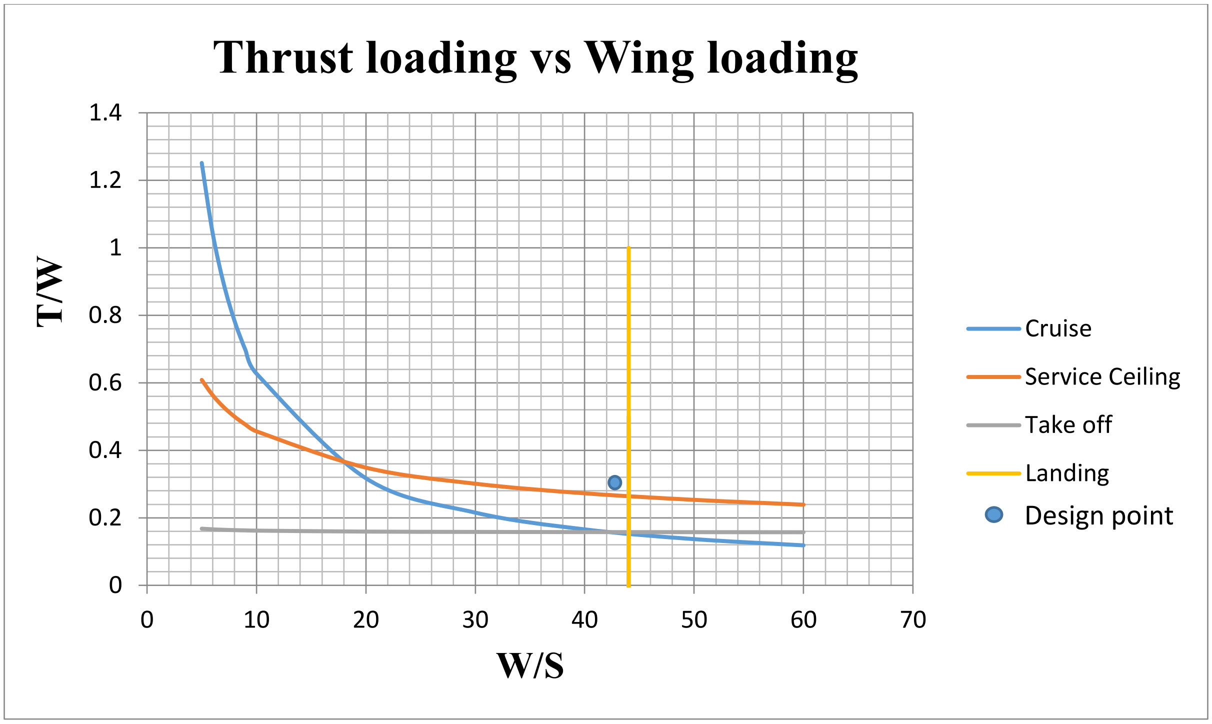

Figure 2: *Constraint diagram*

From the plot, the following results are obtained

Thrust loading: $$\frac{T}{W} = 0.28$$

Wing loading: $$\frac{W}{S} = 43$$

3. Mission Analysis

Mission Analysis was conducted on the Pilatus PC-21 aircraft to estimate the fuel consumption for every stage of the mission using Excel as per the procedure described in [9]. The mission breakdown obtained is represented in Table 8.

Table 8: *Mission breakdown*

Segment Number	Name	Time Estimate (Min)	Estimated Weight after segment (lbm)	Estimated Fuel Usage (lbm)	Fuel Usage (%)	W/W_{to}	W_f/W_i	Fuel left (lbm)
0	Initial		6878			1		815
1	Takeoff	1	6671.66	206.34	25.317	0.97	0.97	608.66
2	Climb to 10,000 ft	3	6571.585	100.074	16.441	0.9554	0.985	508.58
3	Cruise	10	6177.29	394.295	77.527	0.8981	0.94	114.29
4	Descend	2	6152.581	24.7091	21.619	0.8945	0.996	89.58
5	Land	1	6121.818	30.7629	34.340	0.8900	0.995	58.81

3.1 Range

The range has been calculated using Breguet's Range Equation

$$Range = \frac{V}{C_t}\left(\frac{C_L}{C_D}\right)\ln\left(\frac{W_i}{W_f}\right)$$

as per the procedure outlined in [9]. It is calculated to be *1570 NM* at 10000ft. The value of C_t is calculated from values obtained in Cycle analysis.

4. Cycle Analysis

For the cycle analysis of ALTAIR, the design point is taken to be at Sea Level Static Standard Day conditions for take-off as maximum thrust is required for it. GasTurb 12 is used for performing gas turbine engine simulation. The cycle parameters are verified in GasTurb 12 by performing basic cycle analysis as per the data in RFP [1].

ALTAIR is a single shaft, turboprop engine composed of the following components as illustrated in Figure 3.

- Inlet
- Low Pressure Compressor
- High Pressure Compressor
- Combustion Chamber
- High Pressure Turbine
- Free Power Turbine
- Exhaust

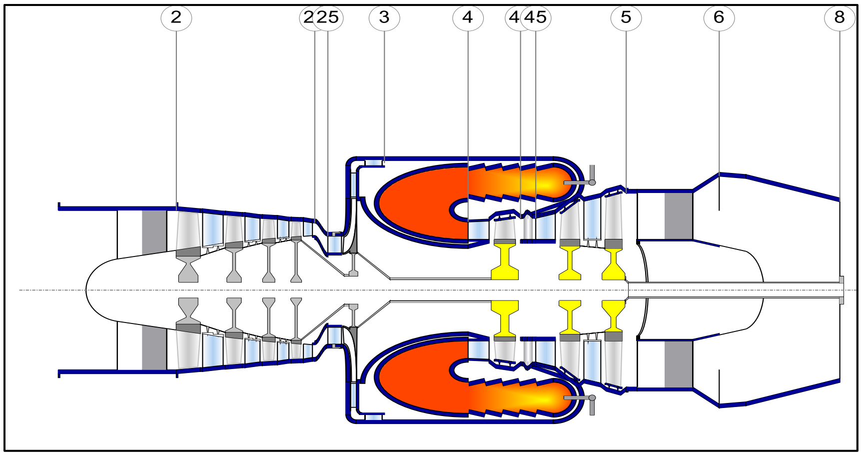

Figure 3: *Engine Flow Path*

According to the RFP [1], it is required that ALTAIR be accommodated within the existing nacelle envelope for compatibility i.e., the maximum diameter of the engine will be 19 inches. Also variable cycle engine designs are not considered as low acquisition cost is a requirement for the new engine so ALTAIR will operate at subsonic conditions at all times [1].

To satisfy these RFP requirements, it was decided to proceed with the same engine model as the current engine i.e., the characteristic reversed flow design of the PT6A model engines to minimize the external changes required and focus on improving the engine performance by implementing currently developed/advanced technology and innovations for various components and parts. These have been described individually for each component in their respective sections.

4.1 Baseline Engine Cycle Analysis

The design point for the baseline engine is taken as take-off over the standard sea level static day. The characteristics of baseline engine PT6A-68B at take-off are shown in Table 9 [2]. Using GasTurb12 the cycle parameters obtained are verified with the data provided in the RFP.

Table 9: *Baseline Engine Characteristics at on-design conditions*

Station	W lb/s	T R	P psia	WRstd lb/s
amb		518.67	14.696	
1	10.580	518.67	14.696	
2	10.580	518.67	14.696	10.580
24	10.580	789.96	51.054	3.758
25	10.580	789.96	51.054	3.758
3	10.580	1091.97	138.917	1.624
31	9.871	606.65	138.917	
4	10.063	2334.95	129.888	2.416
41	10.772	2259.30	129.888	2.544
43	10.772	1768.61	38.351	
44	10.772	1768.61	38.351	
45	10.772	1768.61	38.160	7.660
49	10.772	1491.01	16.945	
5	10.772	1491.01	16.945	15.839
6	10.772	1491.01	16.606	
8	10.772	1491.01	16.606	16.162
Bleed	0.000	1091.97	138.917	

Efficiencies:	isentr	polytr	RNI	P/P
Booster	0.8116	0.8409	1.000	3.474
Compressor	0.8392	0.8594	2.104	2.721
Burner	0.9900			0.935
HP Turbine	0.8552	0.8356	1.577	3.387
LP Turbine	0.8568	0.8436	0.614	2.252

HP Spool mech Eff	0.9990	Nom Spd	36830 rpm
PT Spool mech Eff	1.0000	Nom Spd	30000 rpm
hum [%]	war0	FHV	Fuel
0.0	0.00000	18552.4	Generic

FN	=	4294.76	lb
TSFC	=	0.1608	lb/(lb*h)
V0	=	0.00	ft/s
P25/P24	=	1.00000	
P3/P2	=	9.45	
FN res	=	256.17	lb
Heat Rate	=	11011.6	BTU/(hp*h)
WF	=	0.19184	lb/s
Loading	=	100.00	%
s NOx	=	0.2314	
Therm Eff	=	0.23132	
P45/P44	=	0.99500	
P6/P5	=	0.98000	
A8	=	72.05	in²
P8/Pamb	=	1.13000	
WBld/W2	=	0.00000	
P2/P1	=	1.00000	
driven by HPT			
WCHN/W25	=	0.06700	
WCHR/W25	=	0.00000	
e444 th	=	0.85608	
eta t-s	=	0.74155	
TRQ	=	100.00	%
WCLN/W25	=	0.00000	
WCLR/W25	=	0.00000	
PWSD	=	1164.03	hp
PWSD,eq	=	1320.61	hp
SFC,eq	=	0.52295	lb/(hp*h)

The off-design point for the cycle analysis is the cruise at 10,000 feet. The characteristics obtained using GasTurb 12 is shown in Table 10. This is carried out using mission point analysis in GasTurb 12

Table 10: *Baseline engine characteristics at off-design conditions*

Station	W lb/s	T R	P psia	WRstd lb/s
amb		483.01	10.106	
1	8.875	509.17	12.153	
2	8.875	509.17	12.153	10.633
24	8.875	780.14	42.264	3.785
25	8.875	780.14	42.264	3.785
3	8.875	1084.98	116.876	1.614
31	8.280	602.76	116.876	
4	8.445	2352.39	109.372	2.417
41	9.040	2275.46	109.372	2.544
43	9.040	1782.65	32.312	
44	9.040	1782.65	32.312	
45	9.040	1782.65	32.150	7.660
49	9.040	1467.87	12.366	
5	9.040	1467.87	12.366	18.073
6	9.040	1467.87	12.044	
8	9.040	1467.87	12.044	18.556
Bleed	0.000	1084.98	116.876	

Efficiencies:	isentr	polytr	RNI	P/P
Booster	0.7990	0.8304	0.845	3.478
Compressor	0.8372	0.8580	1.768	2.765
Burner	0.9873			0.936
HP Turbine	0.8547	0.8351	1.317	3.385
LP Turbine	0.8333	0.8157	0.512	2.600

HP Spool mech Eff	0.9990	Speed	36830 rpm
PT Spool mech Eff	1.0000	Speed	30000 rpm
hum [%]	war0	FHV	Fuel
0.0	0.00000	18552.4	Generic

FN	=	1078.94	lb
TSFC	=	0.5496	lb/(lb*h)
V0	=	560.31	ft/s
P25/P24	=	1.00000	
P3/P2	=	9.62	
FN res	=	100.14	lb
Heat Rate	=	9934.3	BTU/(hp*h)
WF	=	0.16473	lb/s
Loading	=	115.97	%
s NOx	=	0.2117	
Therm Eff	=	0.25640	
P45/P44	=	0.99500	
P6/P5	=	0.97396	
A8	=	72.05	in²
P8/Pamb	=	1.19169	
WBld/W2	=	0.00000	
P2/P1	=	1.00000	
driven by HPT			
WCHN/W25	=	0.06700	
WCHR/W25	=	0.00000	
e444 th	=	0.85568	
eta t-s	=	0.70496	
TRQ	=	95.18	%
WCLN/W25	=	0.00000	
WCLR/W25	=	0.00000	
PWSD	=	1107.93	hp
PWSD,eq	=	1287.32	hp
SFC,eq	=	0.46067	lb/(hp*h)

4.2 Sensitivity Analysis

To determine the parameters necessary to bring about the required cycle design improvements, a sensitivity analysis was performed using GasTurb 12.

Table 11: *Effect of various parameters on the engine*

				Shaft Power Delivered	Equivalent Shaft Power	Equivalent SFC	Fuel Flow
	Unit	**Basis**	**Delta**	**%**	**%**	**%**	**%**
Inlet Corr. Flow W2Rstd	lb/s	10.58	2.20462	21.51	21.43	-0.49	20.84
Booster Pressure Ratio		3.474	0.2	-0.2	-0.31	-1.18	-1.49
HP Compressor Pressure Ratio		2.721	1	-2.75	-3.17	-5.53	-8.53
Burner Exit Temperature	R	2334.95	18	2.33	2.16	-0.53	1.62
Number of HP Turbine Stages		1	1	0	0	0	0
Number of PT Stages		2	1	0	0	0	0

From the sensitivity analysis performed, it is concluded that

- With change in mass flow rate, there is an increase in fuel flow while the shaft power increases. So as these compensate each other, change in air flow is avoided.
- With change in the number of stages of the turbine, there is no change in the other parameters. So the number of stages of new turbine is same as the baseline.
- With increase in burner exit temperature, there is a significant rise in power delivered with reduction in ESFC. So the burner exit temperature is increased.
- With increase in pressure ratio of the compressors, there is a significant decrease in fuel consumption. So the pressure ratio is increased.

4.3 Comparison of different cycles

Table 12: *Comparison of different turboprop cycles*

Parameters	**1-spool turboprop**	**2-spool turboprop**	**Boosted turboprop PT**	**Boosted turboprop HP**
ESHP	1837.2	1827.51	1821.47	1806.39
SHP	1649.4	1649.98	1649.65	1648.48
ESFC	0.48001	0.51220	0.48851	0.41702
Overall Pressure Ratio	9.934	10.547	11.60	11.6
Burner Exit Temperature	2606.34	2849.43	2726.23	2458.23

From the above table obtained from optimization studies performed in GasTurb 12, it is observed that the cycle used in baseline engine boosted turboprop on HPT shaft is the most effective design giving the least possible fuel consumption at design SHP. Hence the same cycle is used in ALTAIR.

4.4 Parametric Analysis

Trade-off studies were made using various parameters and carpet plots were obtained for ESFC vs. SHP. The optimized cycle was chosen such that a minimum ESFC was obtained with a minimum of 1600shp of power output. ESFC was chosen as the major design criteria as most of the engine thrust is produced by the propeller and is a standard measure of the efficiency of a turboprop engine.

For the first parametric study, burner exit temperature and pressure ratio were considered as parameters as these are the only modifications that bring about a major improvement in the cycle efficiency [10].

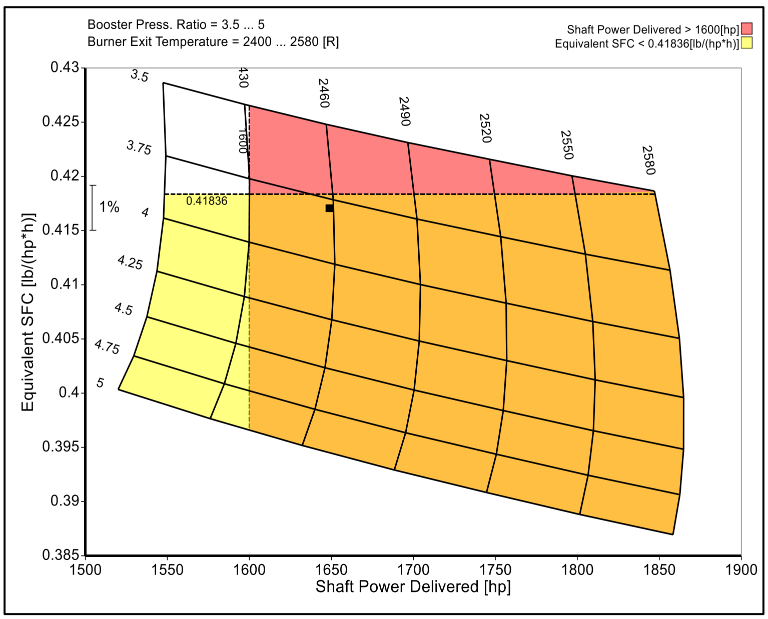

Figure 4: *Contour plot for ESFC vs. SHP*

From the acquired carpet plot, the best possible solution was chosen to extract a minimum of 1600 shp while making sure that a minimum of 20% fuel burn is attained.

The subsequent plots show a design space for further optimization possibilities. This, however, cannot take place as the existing technology limits the maximum pressure ratio that can be attained per stage. The best possible cycle was chosen accordingly.

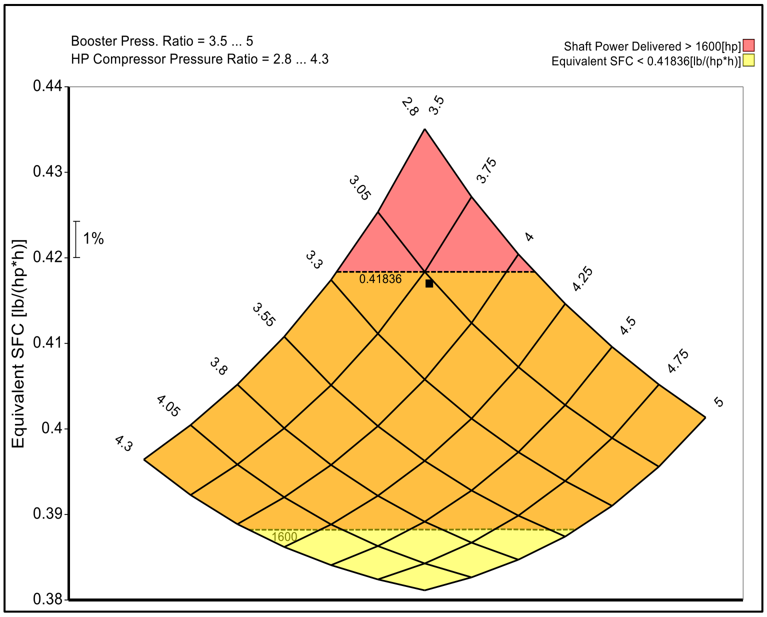

Figure 5: *Contour plot for ESFC vs. SHP*

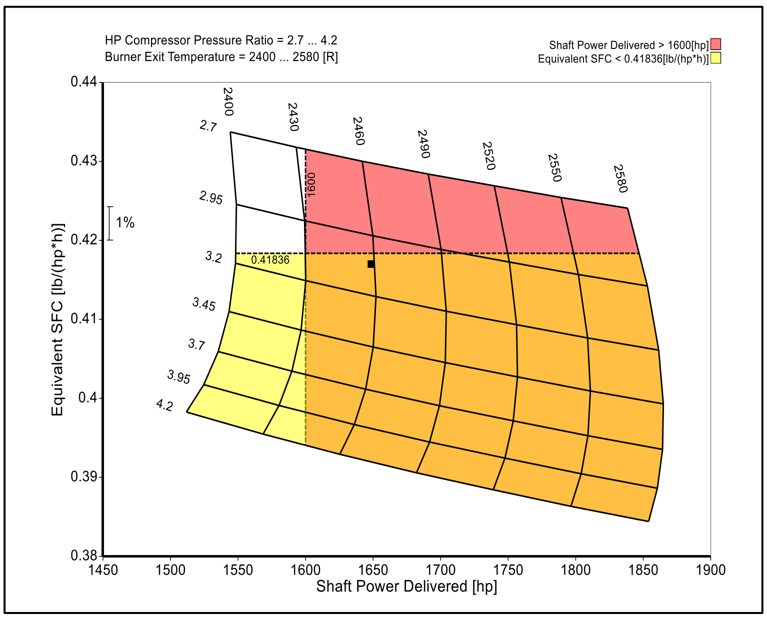

Figure 6: *Contour plot for ESFC vs. SHP*

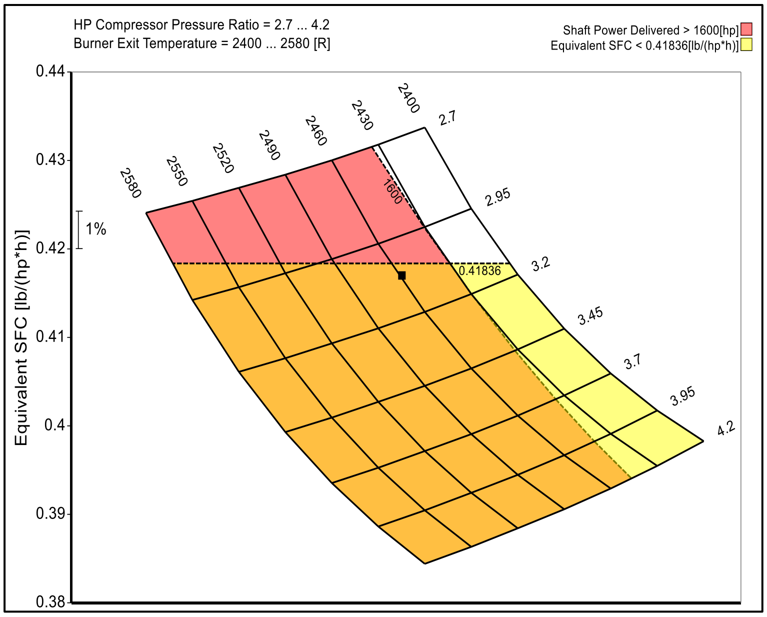

Figure 7: *Contour plot for ESFC vs. SHP*

Essential plots were further made to assure that the cycle point chosen was within the required boundary conditions.

4.5 New Engine Optimization

The RFP solicits that the new engine should be lighter by at least 5% than the current power plant, have an improved fuel burn of at least 20% and should have a power output 25% greater than the baseline so that the payload and/or the range may be extended [1].

From the parametric studies performed above the desired set of values for overall pressure ratio, turbine entry temperature etc. were determined. Keeping the mass flow same as the baseline engine and assuming the polytropic efficiencies of each component as 0.9 an optimized cycle was obtained.

Using ESFC as the main criteria for optimization along with constraints on overall pressure ratio and burner exit temperature based on the technological feasibility and materials chosen, a cycle design was obtained.

Table 13: *ALTAIR characteristics at on-design conditions*

```
             W          T          P        WRstd
Station   lb/s          R       psia         lb/s      FN        =    5333.88 lb
 amb                518.67     14.696
  1      10.580     518.67     14.696                  TSFC      =     0.1412 lb/(lb*h)
  2      10.580     518.67     14.696       10.580     V0        =       0.00 ft/s
 24      10.580     789.61     55.646        3.448     P25/P24   =    1.00000
 25      10.580     789.61     55.646        3.448     P3/P2     =      11.60
  3      10.580    1115.07    170.448        1.338     FN res    =     240.85 lb
 31       9.839     619.48    170.448                  Heat Rate=      8481.3 BTU/(hp*h)
  4      10.049    2458.23    159.369        2.017     WF        =    0.20925 lb/s
 41      10.049    2458.23    159.369        2.017     Loading   =     100.00 %
 43      10.049    1929.79     50.922                  s NOx     =     0.2683
 44      10.049    1929.79     50.922                  Therm Eff=     0.30033
 45      10.049    1929.79     50.668        5.622     P45/P44   =    0.99500
 49      10.049    1514.44     16.945                  P6/P5     =    0.98000
  5      10.049    1514.44     16.945       14.891
  6      10.049    1514.44     16.606                  A8        =      67.74 in²
  8      10.049    1514.44     16.606       15.195     P8/Pamb   =    1.13000
Bleed     0.741    1115.07    170.448                  WBld/W2   =    0.07000
--------------------------------------------           P2/P1     =    1.00000
Efficiencies:    isentr  polytr    RNI    P/P
 Booster         0.8801  0.9000  1.000  3.786          driven by HPT
 Compressor      0.8838  0.9000  2.295  3.063          WCHN/W25 =     0.00000
 Burner          0.9900                 0.935          WCHR/W25 =     0.00000
 HP Turbine      0.9118  0.9000  1.757  3.130          e444 th   =    0.91175
 LP Turbine      0.9118  0.9000  0.737  2.990          eta t-s   =    0.82062
--------------------------------------------           TRQ       =     100.00 %
HP Spool mech Eff 0.9990   Nom Spd   36830 rpm         WCLN/W25 =     0.00000
PT Spool mech Eff 1.0000   Nom Spd   30000 rpm         WCLR/W25 =     0.00000
--------------------------------------------
                                                       PWSD      =    1648.48 hp
                                                       PWSD,eq   =    1806.39 hp
                                                       SFC,eq    =    0.41702 lb/(hp*h)
--------------------------------------------
hum [%]     war0       FHV      Fuel
   0.0   0.00000   18552.4   Generic
```

4.6 Baseline Engine vs ALTAIR

Table 14: *Difference between Baseline engine and ALTAIR*

Cycle Parameter	**PT6A-68B**	**ALTAIR**	**Percent Difference**
Power (ESHP)	1320.61	1806.39	36.78%
SHP	1164.03	1648.48	41.62%
ESFC (lbm/hr/shp)	0.523	0.417	-20.25%
Overall Pressure Ratio	9.45	11.6	22.75%
Tt4 (°R)	2334.95	2458.23	5.28%

Table 14 illustrates the improvements made in the cycle design for a better performance

4.7 Off-design Characteristics of ALTAIR

Properties at off-design point of cruise at 10000 ft. for ALTAIR are shown in Table 15.

Table 15: *ALTAIR characteristics at off-design conditions.*

Station	W lb/s	T R	P psia	WRstd lb/s
amb		483.01	10.106	
1	8.875	509.17	12.153	
2	8.875	509.17	12.153	10.633
24	8.875	779.78	46.059	3.472
25	8.875	779.78	46.059	3.472
3	8.875	1106.96	143.033	1.332
31	8.254	614.98	143.033	
4	8.431	2461.87	133.811	2.017
41	8.431	2461.87	133.811	2.017
43	8.431	1933.13	42.768	
44	8.431	1933.13	42.768	
45	8.431	1933.13	42.554	5.621
49	8.431	1480.60	12.351	
5	8.431	1480.59	12.351	16.950
6	8.431	1480.59	12.031	
8	8.431	1480.59	12.031	17.401
Bleed	0.621	1106.96	143.033	

Efficiencies:	isentr	polytr	RNI	P/P
Booster	0.8664	0.8886	0.845	3.790
Compressor	0.8817	0.8984	1.928	3.105
Burner	0.9872			0.936
HP Turbine	0.9117	0.8999	1.473	3.129
LP Turbine	0.8919	0.8759	0.618	3.446

HP Spool mech Eff	0.9990	Speed	36830 rpm
PT Spool mech Eff	1.0000	Speed	30000 rpm

hum [%]	war0	FHV	Fuel
0.0	0.00000	18552.4	Generic

Parameter	Value
FN	= 1413.22 lb
TSFC	= 0.4523 lb/(lb*h)
V0	= 560.31 ft/s
P25/P24	= 1.00000
P3/P2	= 11.77
FN res	= 83.30 lb
Heat Rate	= 7880.4 BTU/(hp*h)
WF	= 0.17755 lb/s
Loading	= 116.76 %
s NOx	= 0.2444
Therm Eff	= 0.32322
P45/P44	= 0.99500
P6/P5	= 0.97409
A8	= 67.74 in²
P8/Pamb	= 1.19038
WBld/W2	= 0.07000
P2/P1	= 1.00000
driven by HPT	
WCHN/W25	= 0.00000
WCHR/W25	= 0.00000
e444 th	= 0.91165
eta t-s	= 0.78587
TRQ	= 91.32 %
WCLN/W25	= 0.00000
WCLR/W25	= 0.00000
PWSD	= 1505.38 hp
PWSD,eq	= 1684.93 hp
SFC,eq	= 0.37935 lb/(hp*h)

5. Inlet

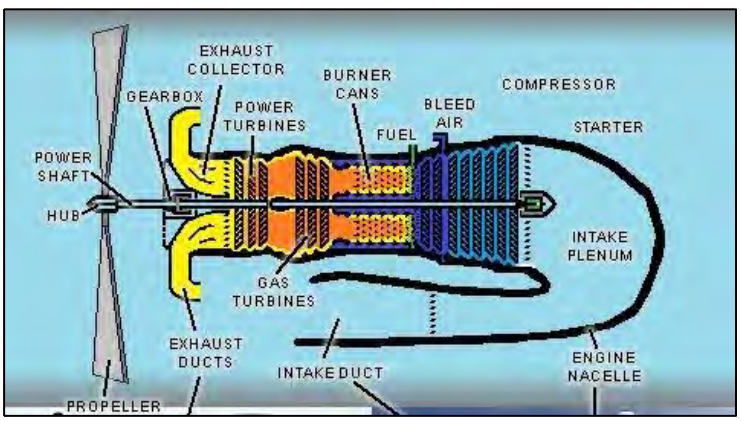

Figure 8: *Basic structure of reverse flow intake [17]*

ALTAIR has reverse flow configuration i.e., air enters the compressor part of gas turbine from rear.

The main benefits of flow reversal are:

- Making the overall engine length smaller.
- Excellent Foreign Object Damage (FOD) protection with inlet buried behind a screen and the air is forced to turn 90º, making an inertial particle separator an obvious solution to FOD.
- Power loss due to employing an extra shaft is undesirable. The simpler option is to turn the engine around so that the power turbine is closest in order to drive the propeller [11].

5.1 Geometry of Inlet Duct

The flow in the subsonic portion of an inlet is dominated by its boundary layer behavior. A subsonic aircraft has an inlet with a relatively thick lip [12].

$$C_{PRideal} = \frac{q_1 - q_2}{q_2} = 1 - \frac{A_1^2}{A_2} = 1 - \frac{1}{AR^2}$$

Here C_{PR} is diffuser pressure recovery. Inlet efficiency is generally characterized by stagnation pressure recovery which is a measure of the available energy in the air that actually goes into the compressor.

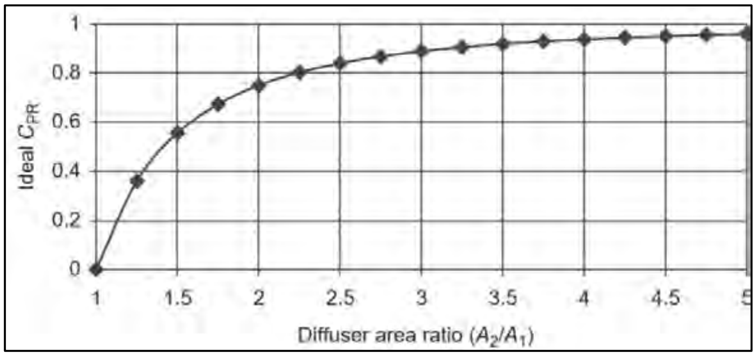

Figure 9: *Ideal C_{PR} vs diffuser Area ratio [12]*

As high static pressure recovery C_{PR} is desirable, large diffuser ratio is preferable. Due to loss of pressure because of boundary layer separation, C_{PR} is taken to be 0.8 [12].

From AxStream calculations, the value of A_2 is found to be 78 in^2.

$$D_{th} = \sqrt{\frac{4}{\pi} A_{thmax}} = \sqrt{\frac{4}{\pi} \left(\frac{m_0\sqrt{T_{t0}}}{P_{t0}}\right)_{max} \frac{1}{MFP@M = 0.8}}$$

This equation is a relation to find throat diameter.

$A_{th\ max} = 30\ in^2$

D_{th}= 0.5 ft or 5.86 in

At cruise condition of 10000ft,

T_{t0}= 483.03 R and P_{t0} = 1462 lbm/ft2

m_0 = 12.43 lbm/s

During the flight, angle of attack of the aircraft will change the angle of the airflow with respect to the centerline of the engine. The largest variations normally occur during the take-off rotation and landing phases of flight.

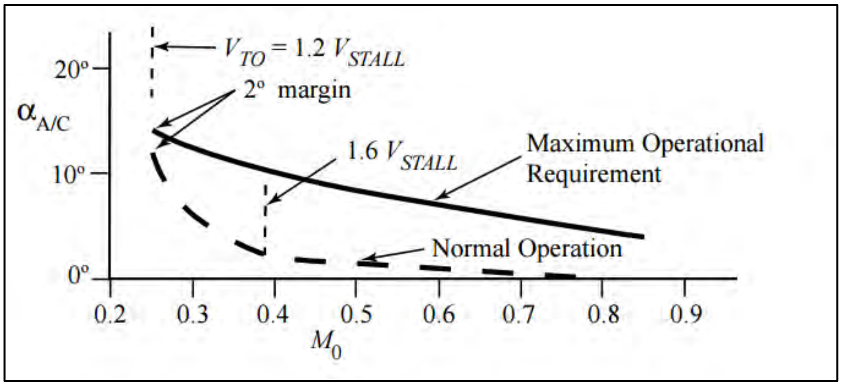

Figure 10: *The variation in angle of attack for a typical subsonic passenger aircraft [12].*

At M_0, $\alpha_{A/C} = 8°$, the incidence of nacelle face can be estimated from [12].

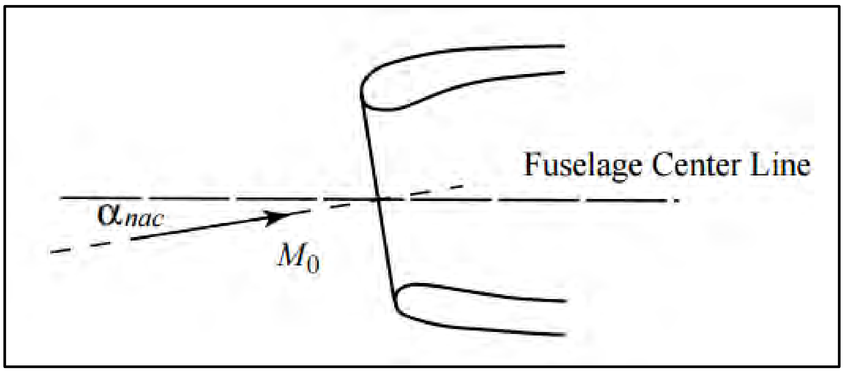

Figure 11: *Inclined nacelle face [12]*

where $\alpha_{A/C}$ is the cruise angle of attack of the aircraft.

For high subsonic speed aircraft, $\alpha_{nac} = 9.3°$

M=0.75 is the upper bound for throat sizing for subsonic inlet. A lower value, say 0.6, is more desirable. The average Mach number at the throat of 0.75 as compared with 0.6 represents a ~12% increase in mass flow rate and nearly the same increase in thrust. The same inlet can thus accommodate a 12% increase in thrust without a need for resizing the inlet [12].

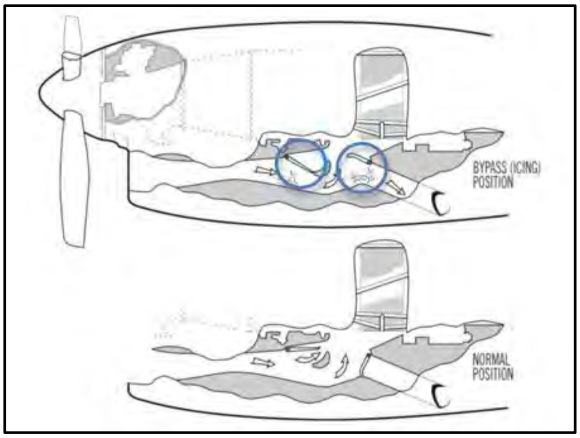

Figure 12: *Representation of air inlet [18]*

Flow distortion and fan stall can be minimized by making the leading edges on the side of the inlet thicker. Design values for D_{hl}/D_{th} range between 1.10 and 1.16 for take-off and landing subsonic aircraft [12].

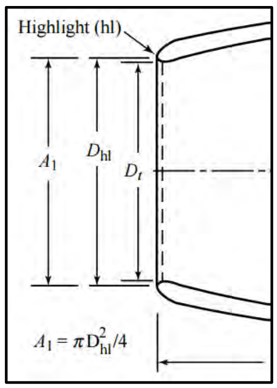

Figure 13: *Inlet Nacelle notations [12]*

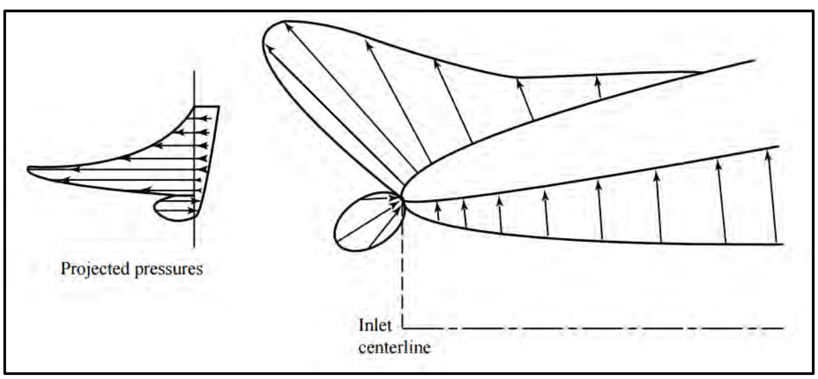

Figure 14: *Pressure distribution around a subsonic inlet lip [13]*

Inlet Flow Distortion: In the presence of the adverse pressure gradient existing in diffusers, boundary layers tend to separate when they are not re-energized rapidly enough by turbulent mixing. Vortex generators can be and are used as mechanical mixing devices to supplement the turbulent mixing. Large capture ratios at take-off and climb pose a potential problem for engine face distortion [12]. Blow-In doors can be employed for extra intake of air during take-off and landing.

FOD Protection: ALTAIR uses Inertial Particle Separator (IPS) to deal with FOD. A radial or tangential component of velocity, prior to ducting, causes a change in flow direction. A U-shaped duct is employed to scavenge off the relatively heavy particles in air due to centrifugal action. Swirl vanes impart a tangential component of velocity to the flow and further enhance separation [14].

Icing Problems: Anti-icing differs from de-icing as the former prevents the formation of ice whereas the latter one dislodges the already formed ice. One possible advantage of de-icing over anti-icing is reduced specific fuel consumption (SFC). An anti-icing is continually operated in order to prevent the formation of ice that consumes large amount of energy which results in a significant SFC penalty. A de-icing system, uses less energy as it is operated at intervals, to keep the formation of ice beyond tolerable levels. Particle separators are incorporated with de-icing system to reduce engine ingestion of ice from the inlet.

De-icing system employed in ALTAIR is Electromagnetic Impulse De-icing (EIDI).This system requires no external additions to the aircraft skin. Current generated from the capacitors is transmitted through flattened, spirally wounded coils. The energy required for EIDI is about 1% of that required for thermal anti-icing of an equivalent area [15].

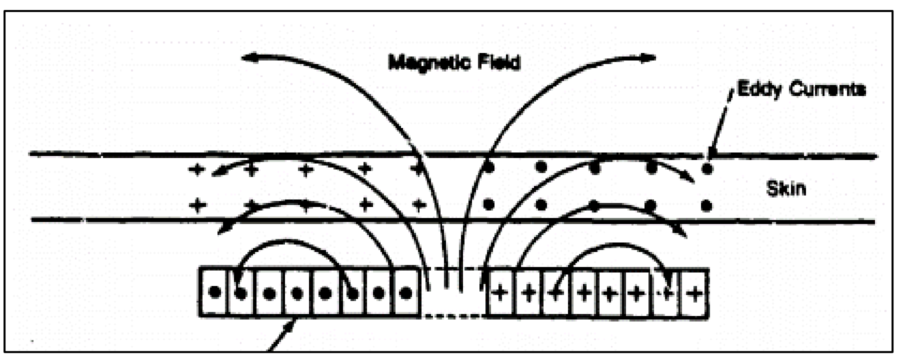

Figure 15: *Formation of Electric current impulse in EIDI [15]*

Acoustic Liners: During aircraft take-off, landing and flight, various types of noise were produced, which is tedious to fully control due to various noise sources and wide frequency range. The most common and effective method used for the reduction of engine noise is the application of acoustic liner which is based on the mechanism of Helmholtz resonator [16]. Acoustic liners are located:

- Between fan face and inlet leading edge
- At fan rotor path

The acoustic liner used in ALTAIR is process control technology or passive noise reduction technology. Airbus A380 is "unusually quiet" during the process of taking off and landing due to the Zero-Splice engine nacelle liner technology. Through improved manufacturing techniques, Airbus has achieved zero-splice intake liner from the A320 's three 3 ×15cm splice, the A340-600 of two 2 × 7.5cm splice, and ultimately to zero splice of A380. Noise reduction attained by this technology is up to 0.4EPNdb and this gives A380 advantage of 10tonnes of weight during take-off [16].

Icing conditions on the liners: Generally, the ice released from the inlet leading edge does not affect the acoustic linings in the area in front of the fan. Ice can build up on the blades of rotor and cause imbalance conditions. The accepted procedure in this situation is to dislodge the ice by increasing the engine speed for a short period [15].

In recent years, Aerospace Research Institute of Materials & Processing Technology has carried out research on the manufacturing of acoustic liner and has achieved good result including the manufacturing technology of high performance fiber reinforced resin matrix composite acoustic liner, precision processing technology, manufacturing technology for micro-perforated composite panel and testing technology [16]. The RAMSES technology featuring an extension of the zero splice concepts is being developed by Airbus and is contributing to improving the efficiency of noise reduction in intake.
These technologies are expected to be incorporated in ALTAIR by 2025.

6. Turbomachinery

A polytropic efficiency of 0.9 was assumed for all the turbomachinery components to generate an optimized cycle for ALTAIR. However, this can be achieved only under ideal conditions where the flow is assumed to be one dimensional isentropic flow. The subsequent design of all the turbomachinery components in AxStream follow actual conditions and is a more practical approach.

6.1 Compressor Design

The compressor system of ALTAIR consists of 4 stage axial compressors and a single stage centrifugal compressor producing an overall pressure ratio (OPR) of 11.6.

Table 16: *Compressor detailed stage and component information*

Compressor	Stage 1	Stage2	Stage 3	Stage 4	Stage 5
Hub to tip Ratio	0.476	0.556	0.65	0.775	NA
	Mean	**Mean**	**Mean**	**Mean**	**Mean**
Lieblein Diffusion Factor	0.574	0.5	0.575	0.459	NA
De Haller Number	0.579	0.638	0.689	0.734	NA
Stage Loading	0.0015	0.0017	0.0018	0.0019	0.0026
Flow coefficient	0.52	0.552	0.584	0.617	0.365
No. of Blades (Rotor)	19	31	37	51	17
No. of Blades (Stator)	37	61	73	91	NA
Solidity	0.94	0.887	1	1.22	1.99
Pitch	0.89	0.633	0.530	0.385	1.02
Axial chord (in)	0.768	0.485	0.352	0.258	0.758
Blade Chord (in)	1.1	0.714	0.531	0.395	0.852
Aspect Ratio	2	2.5	2.5	2.5	1
Taper Ratio	0.8	0.8	0.8	0.8	0.8
Tip Speed (ft/s)	640.379	659.883	675.766	690.857	1476.163
Stagger Angle	44.315	42.835	41.5275	40.916	51.139
Blade Metal angle (inlet)	30.95	31.037	29.512	28.437	41.221
Blade Metal angle (outlet)	57.68	54.633	53.543	53.395	73.057
Velocity triangle (hub, mean and tip)	Page 27-30				
Blade chord	1.982	0.712	0.5279	0.3939	0.8507
Degree of reaction	0.776	0.8	0.825	0.851	0.61
Mach number (absolute)	0.607	0.57	0.544	0.527	0.954
Mach number(relative)	0.646	0.652	0.662	0.677	0.49

6.1.1 Design Procedure

- Owing to our design point, which is the take-off condition at standard sea level static day, we have obtained input values from GasTurb 12 to be used to generate compressor design solutions in AxStream.
- The dimension constraints were set with the mean diameter as reference and complying with the 19” nacelle diameter limit of the engine.
- The design space was obtained as shown in Figure 17.

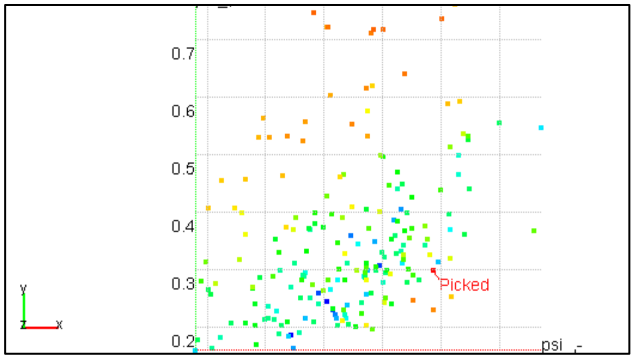

Figure 16: *AxStream Design Space*

- The design space was filtered in order to obtain the design point using the optimum boundary values as shown in Table 17.
- Validated points were chosen according to their total to total efficiency. The design solutions were plotted and compared. Similar procedure was followed for the High pressure compressor.
- After validating the solution space, a trade off was conducted between design points with high total to total efficiency and with conditions close to the design point. Each of these factors were weighed accordingly and the corresponding design point was applied.
- A plot was obtained between inflow of compressor and the outlet pressure and the pressure ratio. The results corresponded with the design conditions and its solutions.
- Post design operations were performed on the applied design point.

Table 17: *Guidelines on the Range of Compressor Parameters [13]*

Parameter	Range of values	Typical value
Flow coefficient ϕ	$0.3 \leq \phi \leq 0.9$	0.6
D-Factor	$D \leq 0.6$	0.45
Axial Mach number M_z	$0.3 \leq M_z \leq 0.6$	0.55
Tip Tangential Mach Number, M_T	1.0–1.5	1.3
Degree of reaction	$0.1 \leq {}^{\circ}R \leq 0.90$	0.5 (for $M < 1$)
Reynolds number based on chord	$300{,}000 \leq Re_c$	>500,000
Tip relative Mach number (1st Rotor)	$(M_{1r})_{tip} \leq 1.7$	1.3–1.5
Stage average solidity	$1.0 \leq \sigma \leq 2.0$	1.4
Stage average aspect ratio	$1.0 \leq AR \leq 4.0$	<2.0
Polytropic efficiency	$0.85 \leq e_c \leq 0.92$	0.90
Hub rotational speed	$\omega r_h \leq 380$ m/s	300 m/s
Tip rotational speed	ωr_t~450—550 m/s	500 m/s
Loading coefficient	$0.2 \leq \psi \leq 0.5$	0.35
DCA blade (range)	$0.8 \leq M \leq 1.2$	Same
NACA-65 series (range)	$M \leq 0.8$	Same
De Haller criterion	$W_2/W_1 \geq 0.72$	0.75
Blade leading-edge radius	$r_{L.E.}$ ~5–10% of t_{max}	5% t_{max}
Compressor pressure ratio per spool	$\pi_c < 20$	up to 20
Axial gap between blade rows	0.23 c_z to 0.25 c_z	0.25 c_z
Aspect ratio, fan	~2–5	<1.5
Aspect ratio, compressor	~1–4	~2
Taper ratio	~0.8–1.0	0.8

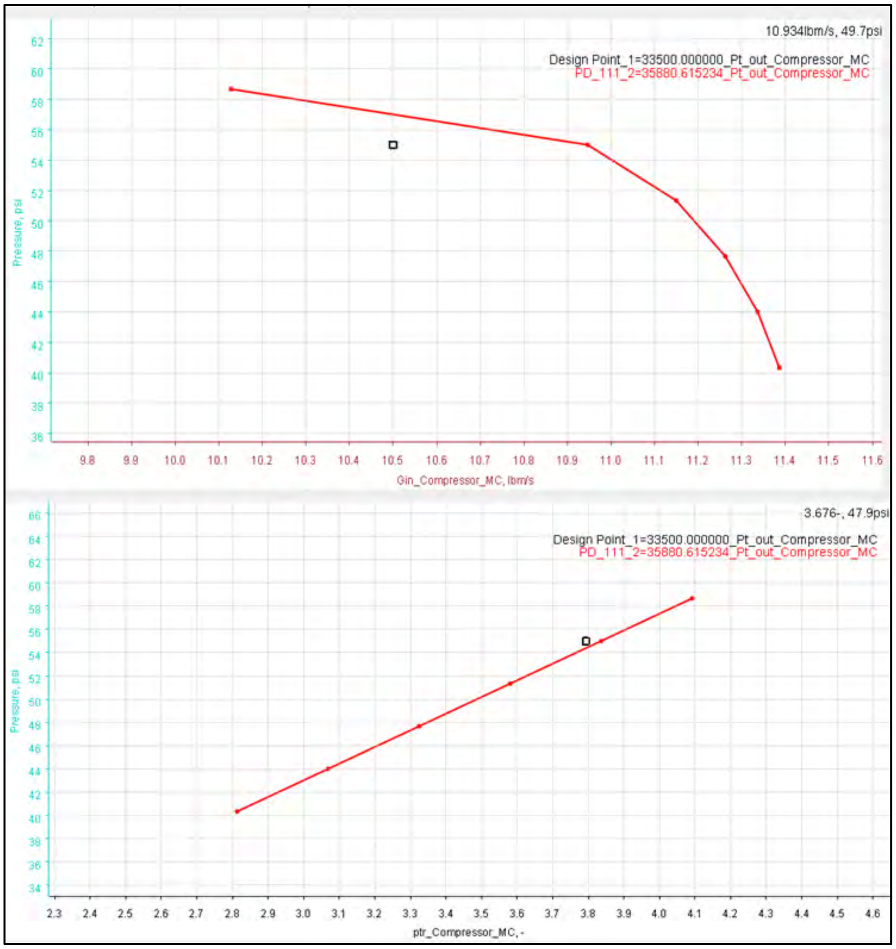

Figure 17: *Preliminary Design Mappings for axial stage*

6.1.2 Post Design and Streamline Analysis

- The whole schematic of the machinery was generated and the flow path was analyzed.
- Shaft rotation speed and the mass flow rate were corrected.
- Variation of parameters was observed and various plots were generated showing the relation of various parameters with stages.
- Dimensions of ALTAIR were optimized and iterations were performed in order to obtain the best possible solution.
- Optimized blade curves were then obtained using streamline analysis.
- The tip diameter of the low pressure compressor was corrected using splines.

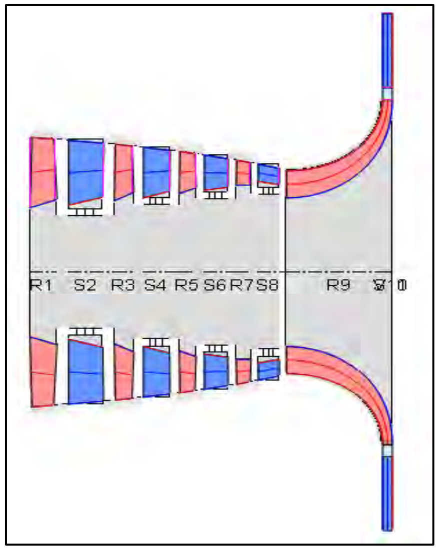

Figure 18: *Flow path of the compressor*

6.1.3 Design Analysis

Compressor stages of ALTAIR were streamlined in order to minimize boundary layer formation. The results obtained by the AxStream analysis illustrates the following optimized design conditions.

- Adverse pressure gradient was avoided which reduces the wake formation within the stages.
- The velocity of air was maintained so that no shockwave is produced.
- Drag coefficient is minimized.
- Temperature and pressure conditions directly affect the blade stresses.

Pressure effect linearly varies with the inlet temperature and reaches up to 18% of the equivalent stress when the inlet temperature in 584.25 K [19]. These variations throughout the flow path indicate the smooth progression of pressure and temperature.

The relative Mach number (of rotor blades) in ALTAIR Compressor is maintained at supersonic conditions as shown in Figure 19(d). This high speed is utilized such that there is no need of inlet guide vanes. This also minimizes tip loading and promotes high pressure ratio stages.

High Pressure compressor module of ALTAIR uses a vaned diffuser. Diffuser slows down the velocity of the fluid flowing through it thereby increasing the pressure drop across it. Implementing a vaneless diffuser would improve the operating range of the centrifugal compressor but its long logarithmic particle spiral path leads to a considerable frictional loss. It also has a diffusion ratio which results in a large diameter requirement. On the other hand, a vaned diffuser has a higher static pressure recovery coefficient leading to greater stage efficiency (upto 4% over the vaneless counterpart) [20].

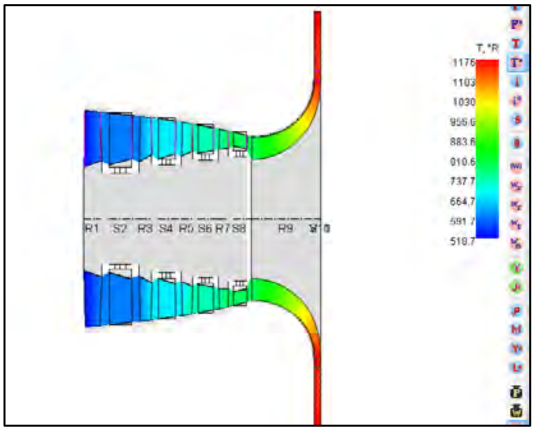

(a)

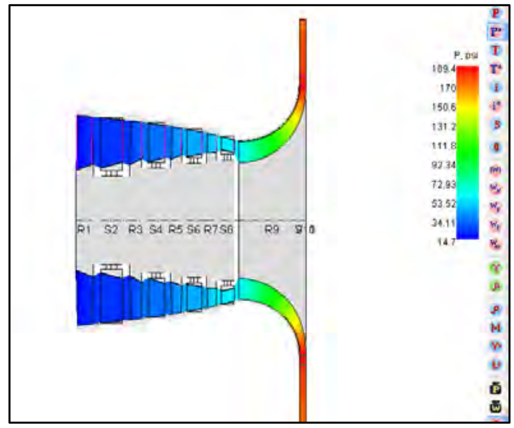

(b)

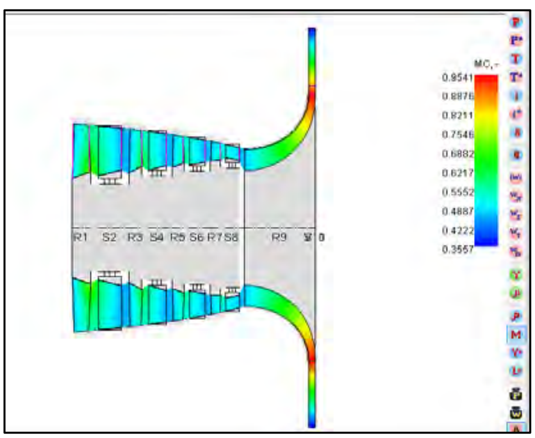

(c)

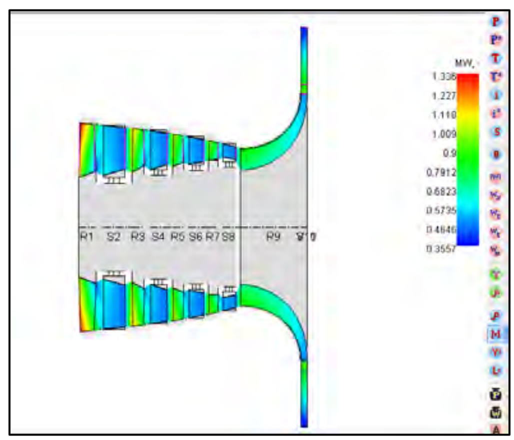

(d)

Figure 19: *Variations of (a) Total temperature, (b) Total pressure, (c) Absolute Mach number, (d) Relative Mach number throughout the designed compressor*

6.1.4 Hub-to-Tip Ratio

Table 18: *Hub to tip ratio of LPC stage*

	Rotor 1	Rotor 2	Rotor 3	Rotor 4
Hub diameter	4.040	4.472	4.930	5.466
Tip diameter	8.472	8.040	7.583	7.046
Ratio	0.476	0.556	0.650	0.775

ALTAIR also uses sets of de-swirlers in the centrifugal compressor stages, which increases the overall efficiency by minimizing the frictional losses [21].

6.1.5 Enthalpy-Entropy Curves

The thermodynamic effect on compressor efficiency can best be understood by considering the enthalpy-entropy diagram across all the stages. It also gives an integrated picture of total to total efficiency, kinetic energy, pressure rise across a stage, losses and extent of change due to irreversibility.

The total enthalpy rise on the mean line of axial stage of ALTAIR is 151.574 kJ/kg while that on the mean line of centrifugal stage is 216.451 kJ/kg.

Table 19: *Enthalpy and Entropy rise in LPC and HPC*

	Stage 1	Stage 2	Stage 3	Stage 4	Stage 5
Enthalpy rise (kJ/kg)	43.901	39.896	35.891	31.886	216.451
Entropy rise (J/kg K)	14.136	13.695	10.712	9.034	51.675

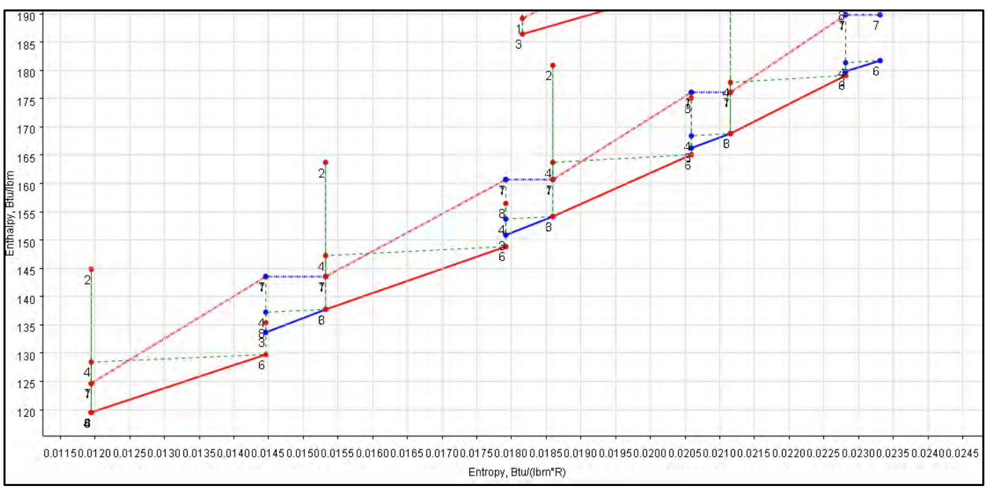

Figure 20: *Enthalpy vs Entropy (LPC)*

6.1.6 Velocity Triangles

Velocity triangles were obtained from AxStream after optimizing various parameters. Following figures (Figure 21, 22, 23) shows the velocity triangles at different sections of the blades of the compressor (both LPC and HPC). Figure 24 shows the velocity view of the rotors and stators of various stages.

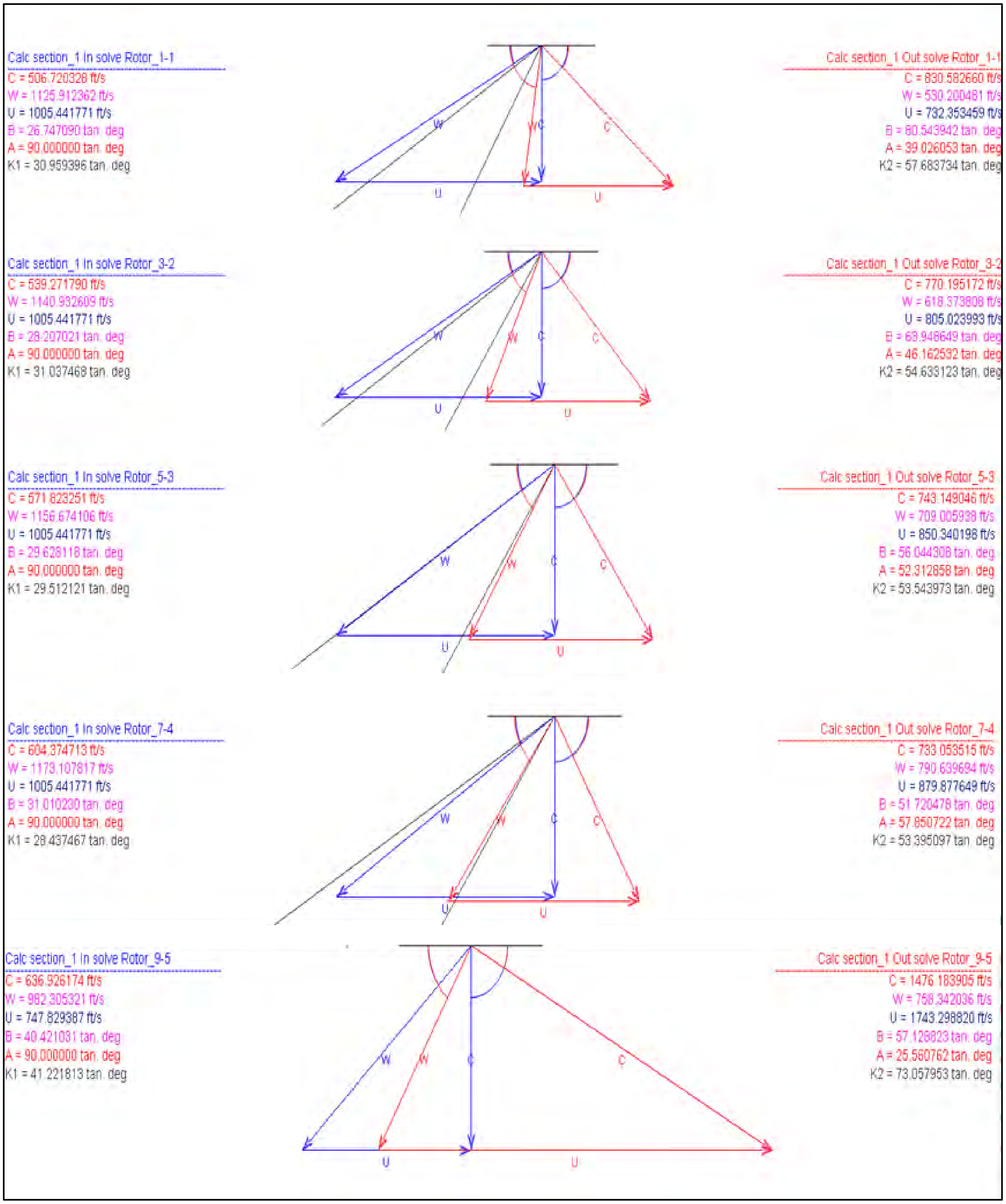

Figure 21: *Velocity triangles at Compressor hub*

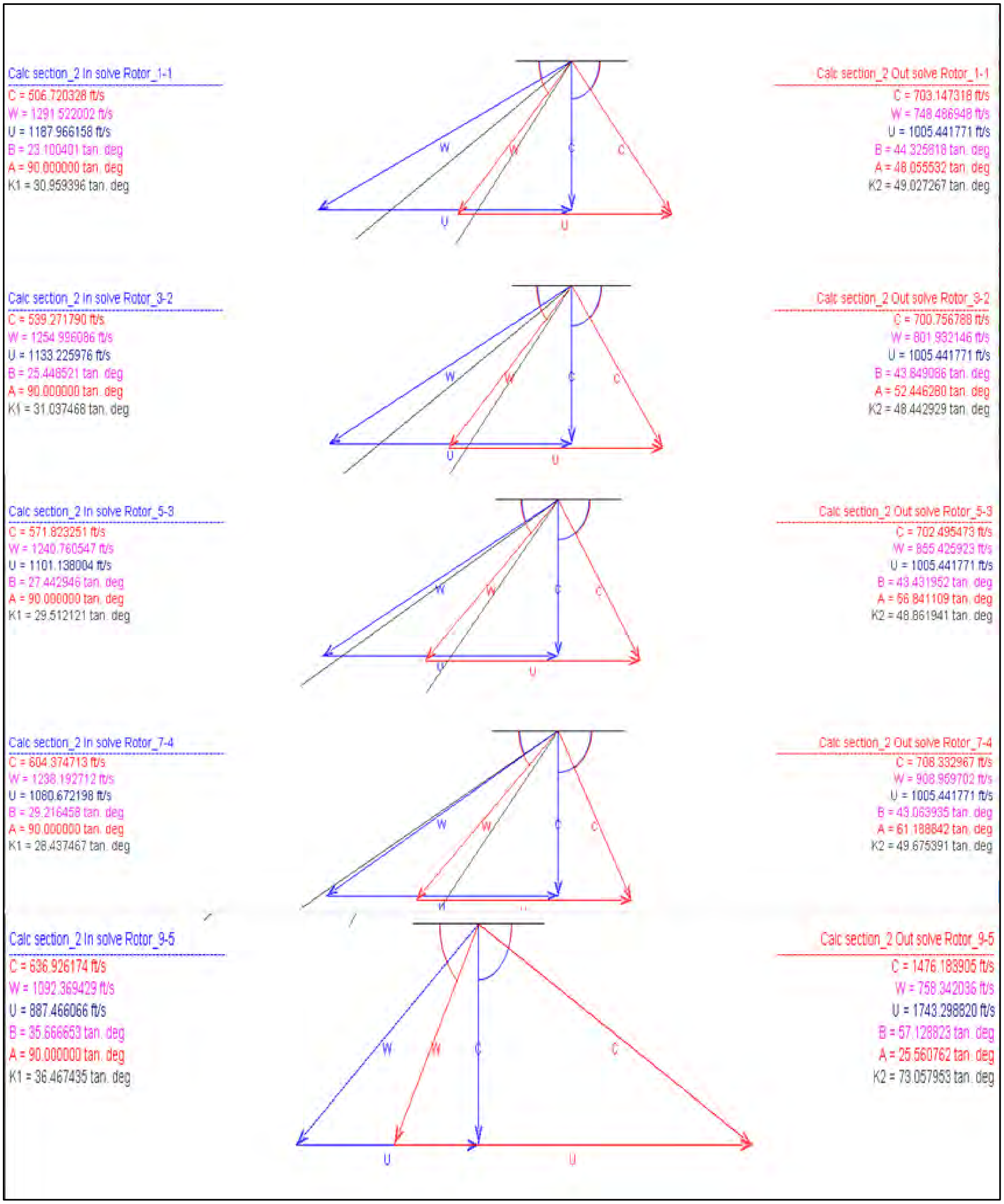

Figure 22: *Velocity triangles at Compressor mean line*

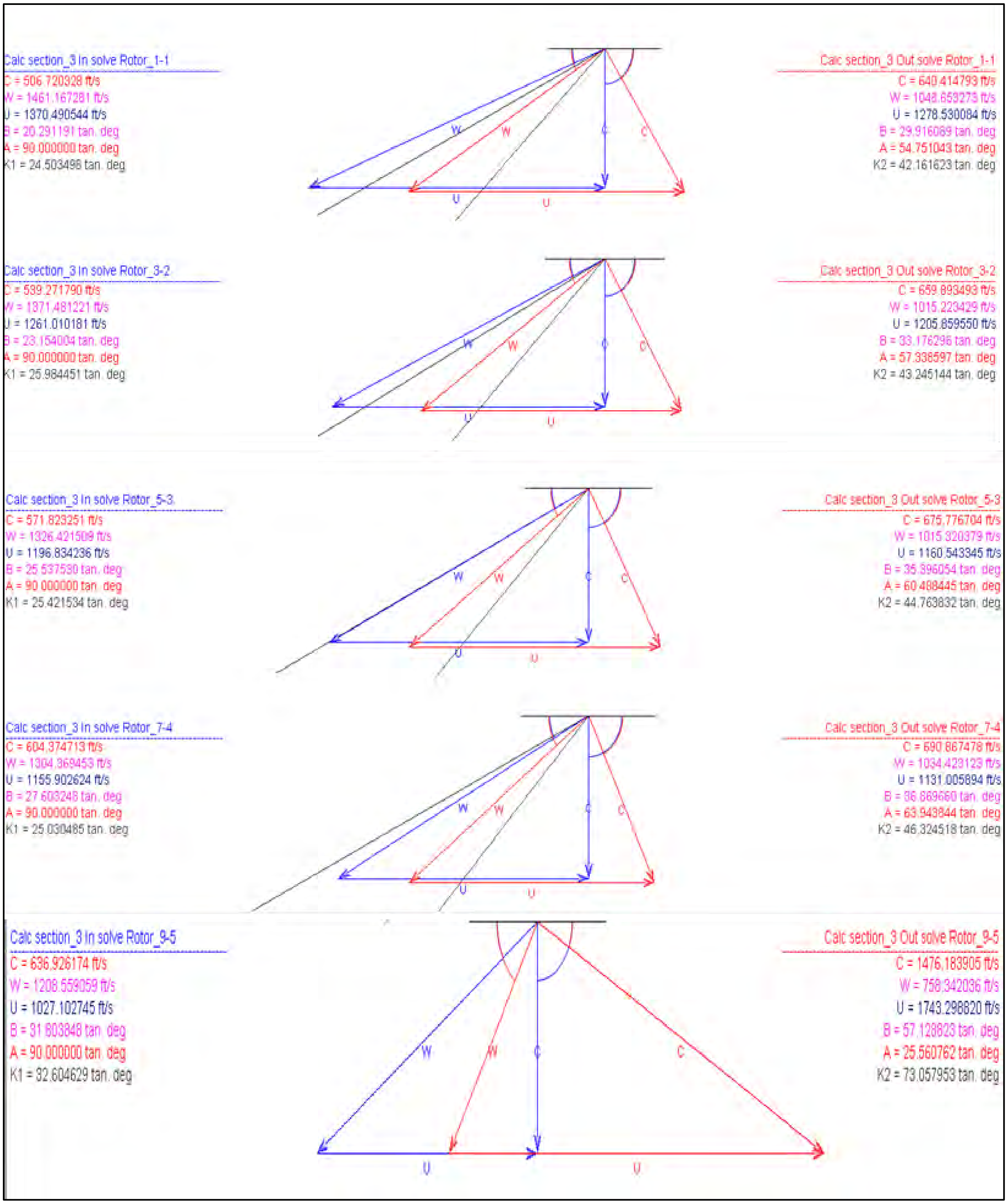

Figure 23: *Velocity triangles at Compressor tip*

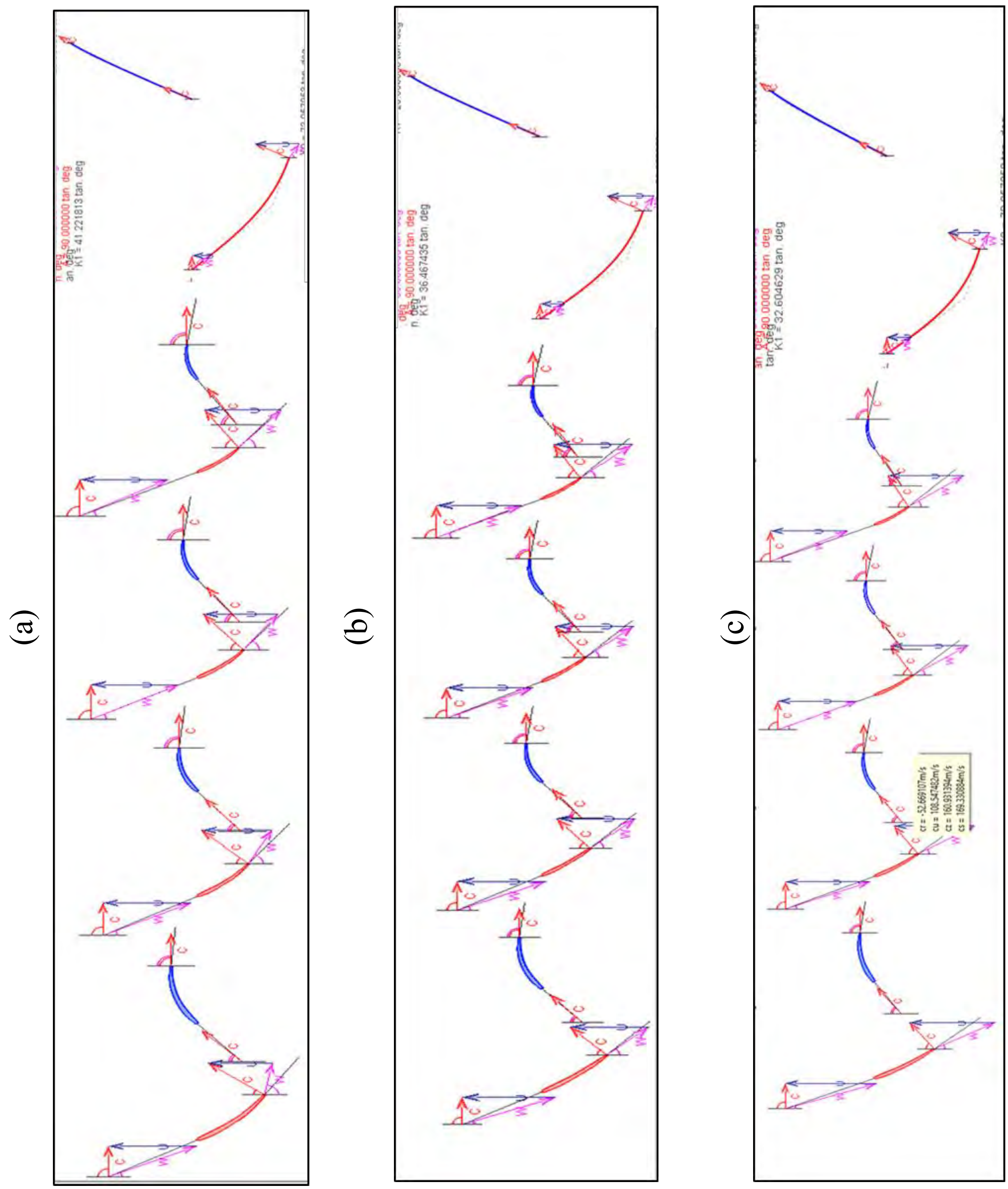

Figure 24: *Velocity view at stators and rotors of compressors at a) hub, b) mean and c) tip*

6.1.7 Blade Profiling

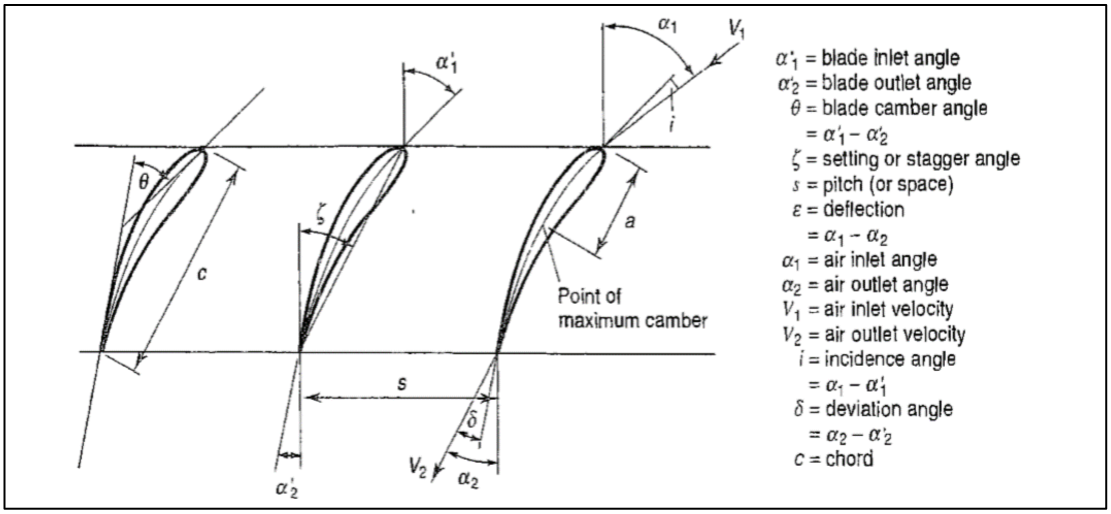

Figure 25: *Cascade notations [10]*

Figure 25 represents the basic notation of a cascade. AxStream and Excel iterations were done to find the optimum values of solidity and number of blades. Table 21 summarizes the values of parameter of rotors for each stage. The value of solidity is seen to be near 1 and the β_1=30°. From Table 20, we select NACA 65-(18)10.

NACA 65-(18)10 represents the 65-series camber shape that produces an isolated theoretical (i.e., inviscid) lift coefficient of 1.8 (at zero angle of attack) and has a 10% thickness-to-chord ratio [13].

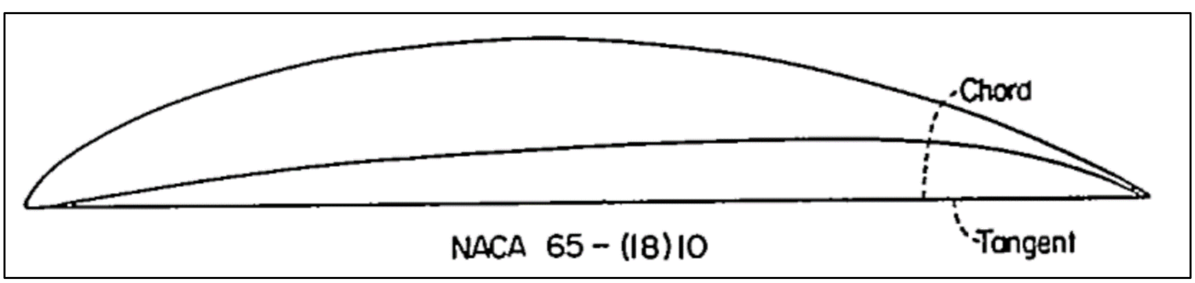

Figure 26: *NACA 65-(18)10 profile [22]*

Table 20: *Solidity vs inlet flow angle [22]*

σ	NACA airfoil			
	$\beta_1=30°$	$\beta_1=45°$	$\beta_1=60°$	$\beta_1=70°$
0. 50		65–410 65–(12)10 65–(18)10	65–410 65–(12)10 65–(18)10	
. 75		65–410 65–(12)10 65–(18)10	65–410 65–(12)10 65–(18)10	
1. 00	65–010 65–410 65–810 65–(12)10 65–(15)10 65–(18)10	65–010 65–410 65–810 65–(12)10 65–(15)10 65–(18)10 65–(21)10 65–(24)10 65–(27)10	65–010 65–410 65–810 65–(12)10 65–(15)10 65–(18)10 65–(21)10	65–010 65–410 65–810 65–(12)10 65–(15)10
1. 25	65–410 65–(12)10 65–(18)10	65–410 65–(12)10 65–(18)10	65–410 65–(12)10 65–(18)10	65–410 65–810 65–(12)10 65–(15)10
1. 50	65–010 65–410 65–810 65–(12)10 65–(15)10 65–(18)10	65–010 65–410 65–810 65–(12)10 65–(15)10 65–(18)10 65–(21)10 65–(24)10	65–010 65–410 65–810 65–(12)10 65–(15)10 65–(18)10 65–(21)10 65–(24)10	65–010 65–410 65–810 65–(12)10 65–(15)10

Table 21: *Parameters of Compressor blades*

Parameters	**Stage 1**	**Stage 2**	**Stage 3**	**Stage 4**	**Stage 5**
Blade inlet angle*	30.95	31.037	29.512	28.437	41.221
Blade outlet angle*	57.68	54.633	53.543	53.395	73.057
Air inlet angle*	26.74	28.207	29.628	31.01	40.421
Air outlet angle*	80.54	63.948	56.044	51.72	57.128
Blade height*(in)	2.2	1.78	1.326	0.79	0.85
mean radius*(in)	3.13	3.128	3.128	3.1283	2.76
Solidity	0.94	0.887	1	1.22	1.99
Aspect ratio	2	2.5	2.5	2.5	1
No. of blades	19	31	37	51	17
Pitch(in)	0.89	0.6337	0.5309	0.3852	1.02
Taper Ratio	0.8	0.8	0.8	0.8	0.8
Mean Chord(in)	1.982	0.712	0.5279	0.3939	0.8507

**shows the parameters taken from AxStream solution*

The analytical methods used to estimate solidity, AR, pitch, mean chord and number of blades were derived from [10]. The typical value of Aspect ratio can be 2-4 and should not be less than one. The chord chosen for first stage of rotor is determined by stringent requirements for FOD resistance. This is often the case for aircraft engines, and therefore, first stages usually have an aspect ratio lower than optimum AR.

6.1.8 Compressor Blade Materials

Following parameters have to be considered for deciding the adequate material for the compressor blades.

- Temperature tensile strength
- Creep properties
- Stress rupture life
- High cycle fatigue (HCF)
- Corrosive and Oxidative properties
- Overstress
- Mass density
- Manufacturability
- Cost

HCF can have multiple sources which can severely affect the working of the gas turbine engine of the aircraft. Aerodynamic excitations caused to changing pressures at high altitudes and component vibrations are the main sources for cycle fatigue in compressor and turbine blades [24].Turbine blades also bear the highest temperatures than any other rotating components. The temperature in ALTAIR may go upto 1200°C. The airfoil root has to withstand maximum stresses as they undergo the maximum centrifugal loads. The blades are also exposed to the high temperature oxidation environment and hot corrosion. Hot corrosion is generally categorized as Type 1 corrosion (800-950°C) and Type 2 corrosion (600-750°C) [23,24].

Material Selection: There has been a substantial development in material selection for compressor and turbine blades.

- Super-alloys
- Coatings
- Titanium Aluminides (Ti_2AlNb)
- Chromium based alloys

- Molybdenum based alloys.
- Platinum based alloys.
- Titanium based alloys

Table 22: *Trade-off study between different types of compressor materials.*

Super-alloys	**Cr alloy**	**Mb Alloy**	**Pt alloy**	**Ti alloy**
Retain strength at higher temperatures.	High melting point.	Work efficiently around 1100°C.	Temperature range can exceed upto 1700°C.	Good high temperature mechanical properties.
Faster oxidation.	Good oxidation resistance.	Silicide & boride provide oxidation resistance.	High melting point.	High melting point.
		Enhanced creep resistance.	Thermal shock resistant.	Superior corrosion resistant.
		Super-plasticity at high temperature	Research required for practical use.	Very high strength to weight ratio.

The compressor blades and guide vanes of ALTAIR are made up of Ti6246. This material is also superior to the conventional Ni based super-alloys in terms of creep resistance and density.

Table 23: *Properties of Ti6246 [25]*

Ultimate tensile strength	174000 psi
Yield tensile strength	152000 psi
Modulus of elasticity	16500 ksi
Poisson's Ratio	0.33
Shear Modulus	6220 ksi
Thermal Conductivity	0.203 BTU-in/hr-ft²-°R @ Temperature 1460°R
Melting point	3370 °R

Thermal Barrier Coatings: ALTAIR uses a thermal barrier coating of Y_2O_3, also known as YSZ. As shown in the AxStream analysis of ALTAIR, the rotors and the stators experience different amount of pressure and temperature. Therefore, a 150µm thick layer has been imposed over rotating components while a 400µm thick layer has been imposed over stators in compressors [28].

ALTAIR also uses a protective layer "smart coating" of NiCoCrAlY, which protects the blades from getting oxidized at higher temperatures as well as from both the types of hot corrosion. Alumina scales are effective against high temperature oxidation and type 1 hot corrosion while Chromia scales are effective against type 2 hot corrosion. The outer surface is composed of Al rich coating which provides protection at higher temperature ranges while the inner layer is composed of Cr rich coatings to provide the same at lower temperatures [26, 27].

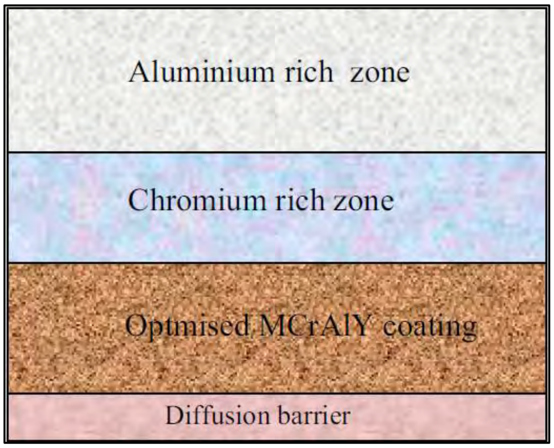

Figure 27: *A schematic representation of microstructure of a smart coating [26]*

Smart coating increases the life of blades significantly. It also enhances the life of TBC as it depends on the life of bond coatings.

Table 24: *Effect of coating [26]*

Type of coating	**Life (in hours)**
Uncoated super-alloy	<2
Smart coating	300
Smart coating + 100µm TBC	910
Smart coating + 400µm TBC	1170

6.1.9 Stress Analysis

The rotor blades at each stage must withstand centrifugal, bending, vibrational, and thermal stresses. The governing stress in the rotor design, is centrifugal stress. If the 1^{st} stage rotor blades have an appreciable factor of safety for centrifugal loading, it can be assumed safe for all types of loadings. The equation that governs the centrifugal stress is:

$$\sigma_c = \rho_{blade} \frac{\omega^2 A}{4\pi} (1 + \frac{A_t}{A_h})$$

Table 25: *1st stage rotor structural analysis*

Design Parameter – Rotor, 1st Stage	Value
Allowable centrifugal stress, σ_{all} (psi)	145037.7
Material density (lbm/in^3)	0.164
Taper ratio	0.8
HPC angular speed ω (rpm)	36830
Flow Area, A (in^2)	43.506
Design Centrifugal Stress, σ_c (psi)	39360.17
Safety factor	3.68

AxStress Results of 1st stage rotor blade: The stress distribution of 1st blade rotor is shown in Figure 27 and the maximum stress obtained is 84847.076 psi as shown in Figure 28. The allowable stress for Ti6246 is 145037 psi. The margin of safety is 2. Therefore, it has been concluded that 1st blade of rotor of HPC is safe with appreciable margin and this could be compensated by FOD effect on blades.

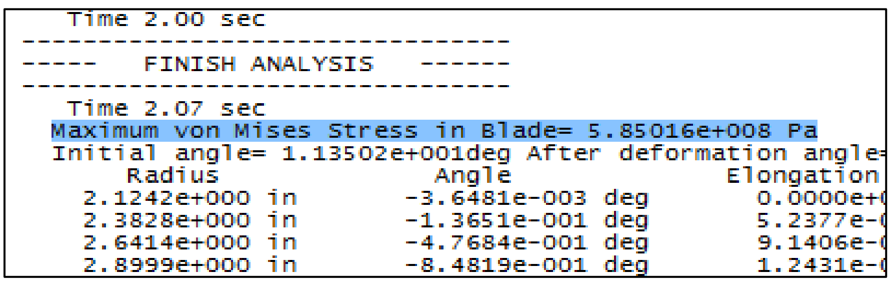

Figure 28: *Maximum Stress on blade*

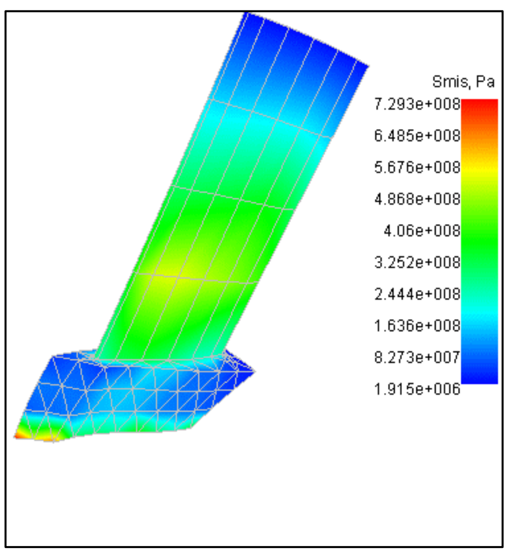

Figure 29: *Von-Mises Stress concentration*

6.2 Turbine Design

ALTAIR's turbine section consists of a single stage high pressure turbine (HPT) and two stage low pressure turbine (LPT) similar to that used in the current baseline engine. Pressure compounded (Rateau stage) reaction turbine is the design choice for both the high pressure and low pressure modules.

Following the same design procedure as that of compressors in AxStream as stated in section 6.1.1, and using the default parameters for losses, the turbine design solutions were obtained. Due to the advanced materials used for the turbine materials as mentioned in section 6.2.4, cooling is not required.

An optimization process was performed to edit the flow path. This inverse design task involves

- Using a constant specific diameter and corresponding spline adjustment
- Mollier diagram editing- This can be used to redistribute heat drop between vanes and blades by changing the degree of reaction.

The HPT which drives the compressors results in a total-to-total pressure ratio of 3.129 with an internal total-to-total efficiency of 85.7% and the LPT generates the pressure ratio of 2.99 and is 90.8% efficient.

Free Vortex design approach is implemented for all the turbine stages where the specific enthalpy rise across the blade is constant. This assumption results in the shape of the velocity triangles varying from root to tip of the blade as the blade speed increases with radius [10].

Table 26 represents the detailed stage and component information of the turbine section in ALTAIR obtained from AxStream.

Table 26: *Turbine detailed stage and component information*

Turbine	**Stage 1 (HPT)**	**Stage 2 (LPT)**	**Stage 3 (LPT)**
	Mean	**Mean**	**Mean**
Zweifel Coefficient	0.884	0.753	0.758
Taper Ratio	0.8	0.8	0.8
Specific Work (Btu/lbm)	149.007	47.697	68.475
Stage Pressure Ratio	3.043	1.495	1.973
Degree of Reaction	0.696	0.535	0.442
Velocity Triangle (hub, mean and tip)	Page 40, 41	Page 43, 44	Page 43, 44
Aspect Ratio	3	3	3
AN2	1.84E+17	4.50E+16	1.00E+17
Number of Blades (rotor)	102	86	84
Number of Blades (stator)	85	72	70
Axial Chord (in)	0.298	0.298	0.227
Blade Chord (in)	0.331	0.317	0.343
Blade Metal angle (Rotor Outlet)	13.452	25.071	23.187
Mach number (Absolute)	0.443	0.317	0.32
Mach number (Relative)	1.211	0.729	0.762
Tip speed (ft/s)	878	639.35	581.22
Flow coefficient	0.353	0.421	0.36
Pitch (in)	0.337	0.413	0.441
Cooling flow detail	NA	NA	NA

Velocity triangles were obtained for turbines from AxStream in a similar way as that of compressors. Following figures (Figure 31, 32, 33) shows the velocity triangles at different sections of the blades of the turbine (both HPT and LPT).

Figure 34, 40 shows the velocity view of the rotors and stators of various turbine stages.

6.2.1 High Pressure Turbine

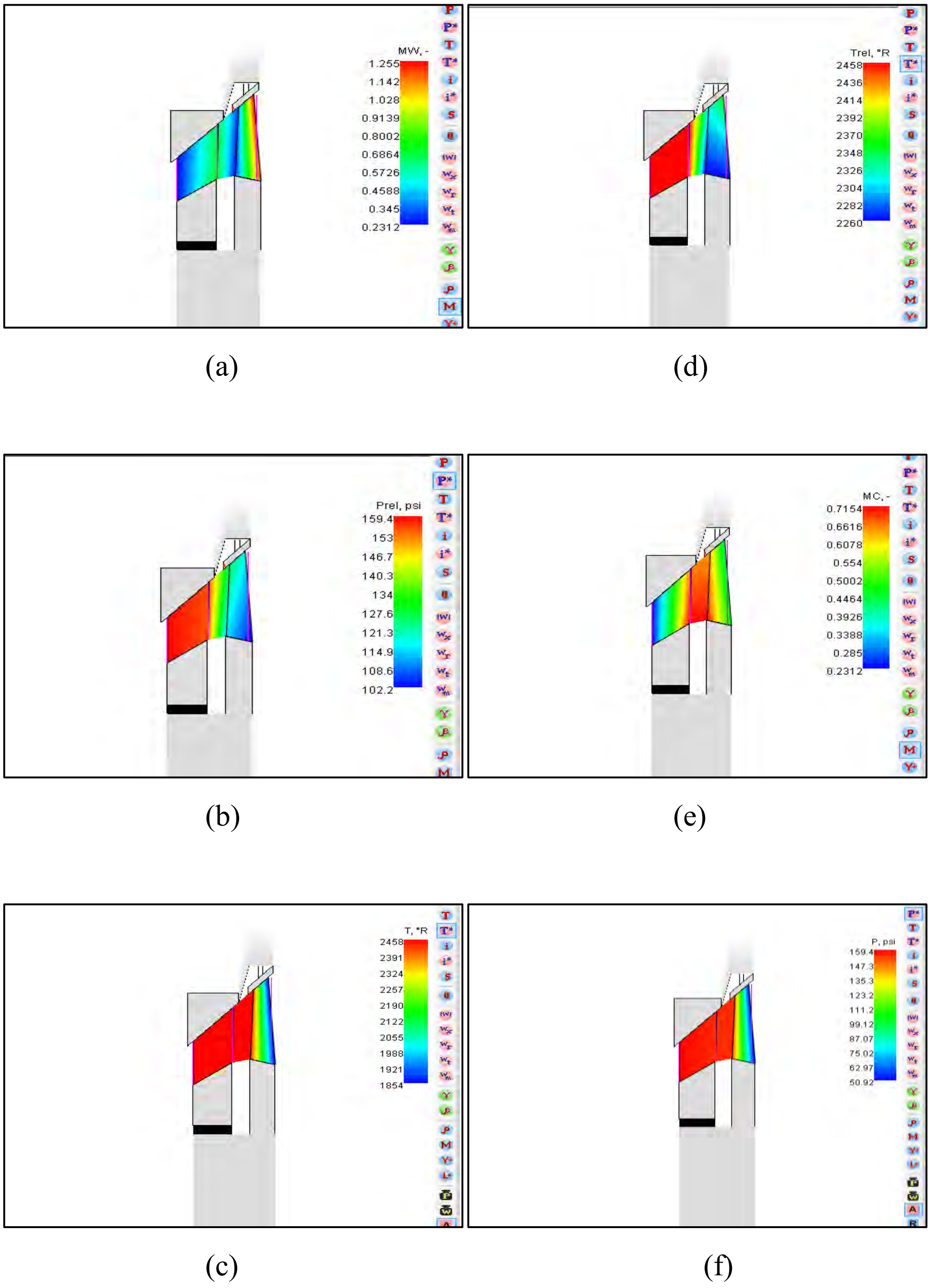

Figure 30: *Variation of (a) Relative Mach number, (b) Relative total pressure, (c) Total temperature, (d) Relative total temperature, (e) Absolute Mach number, (f) Total pressure throughout the HPT*

6.2.1.1 Velocity Triangles

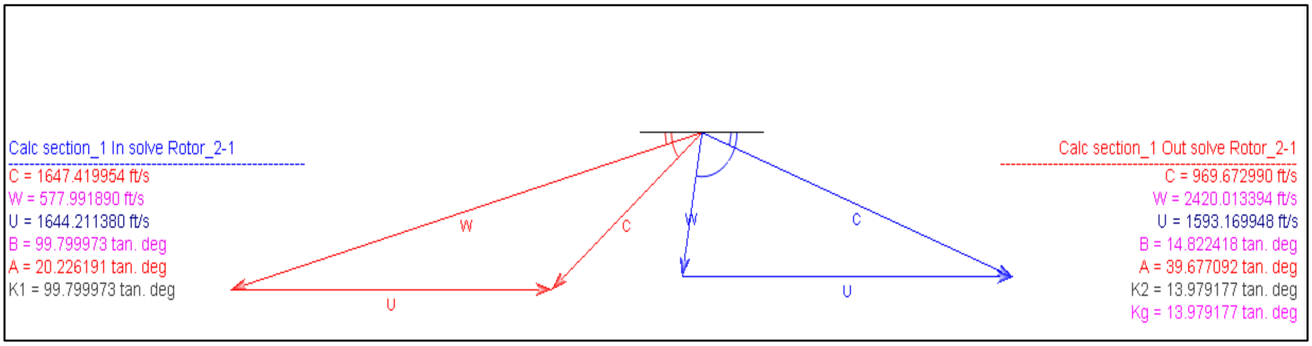

Figure 31: *Velocity triangles at HPT hub.*

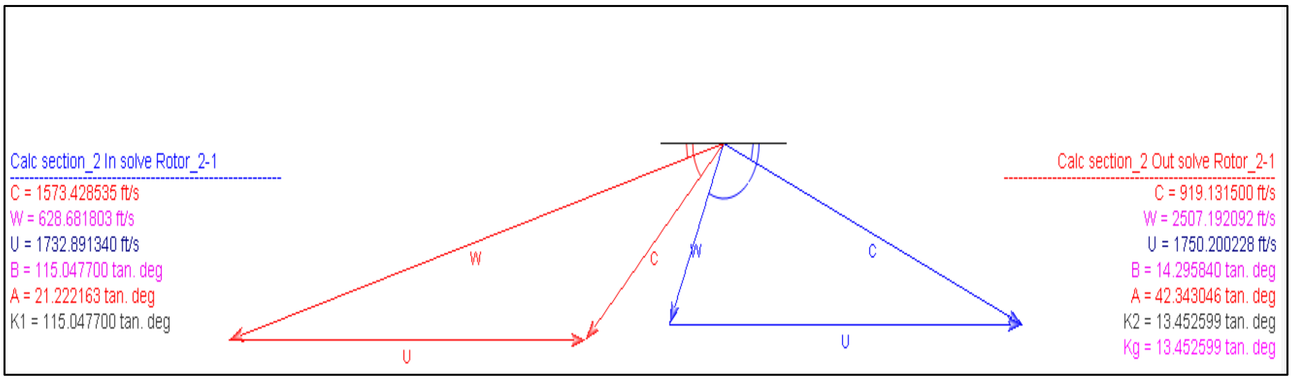

Figure 32: *Velocity triangles at HPT mean line.*

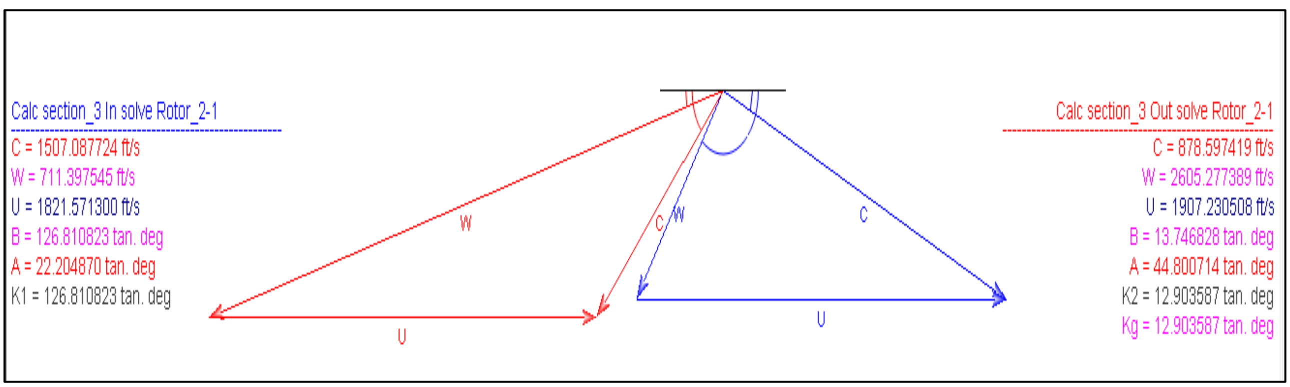

Figure 33: *Velocity triangles at HPT tip.*

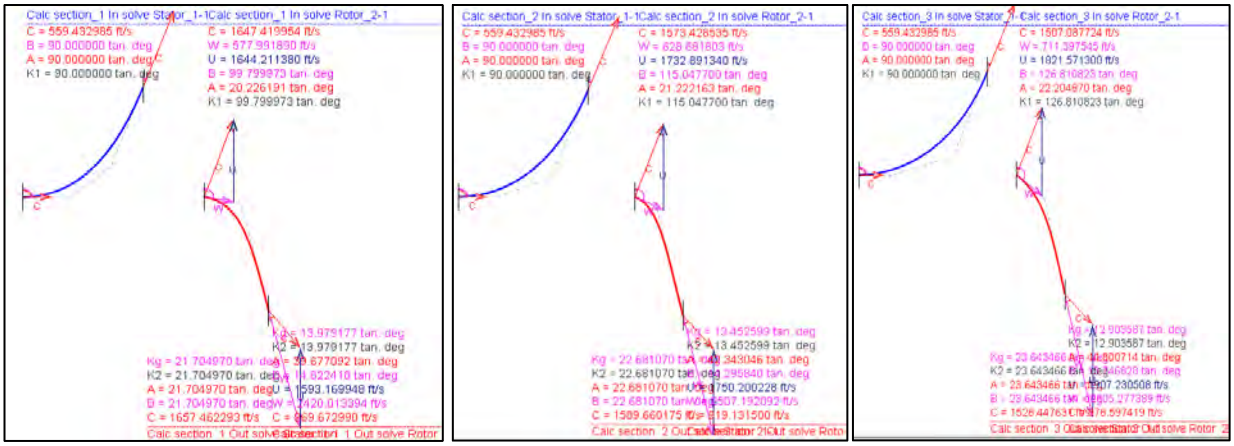

(a) (b) (c)

Figure 34: *Velocity view at stators and rotors of HPT (a) Hub, (b) Mean, (c) Tip*

6.2.2 Low Pressure Turbine

Variation of parameters:

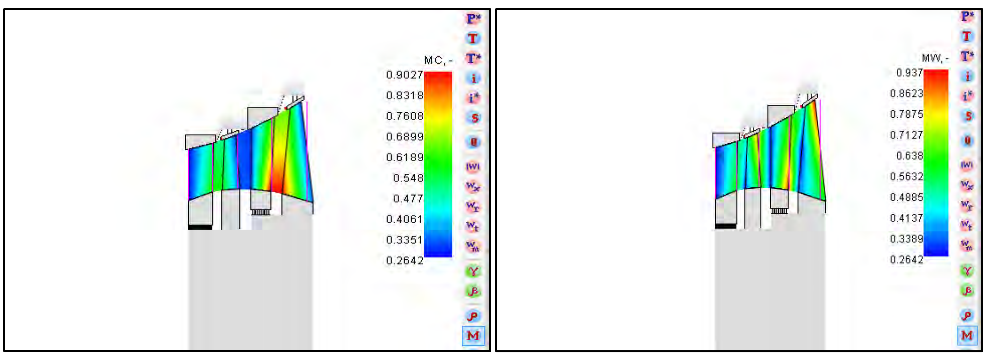

(a) (d)

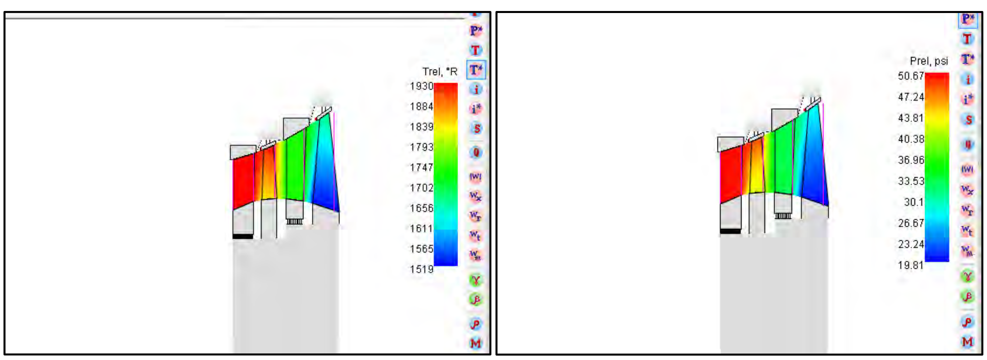

(b) (e)

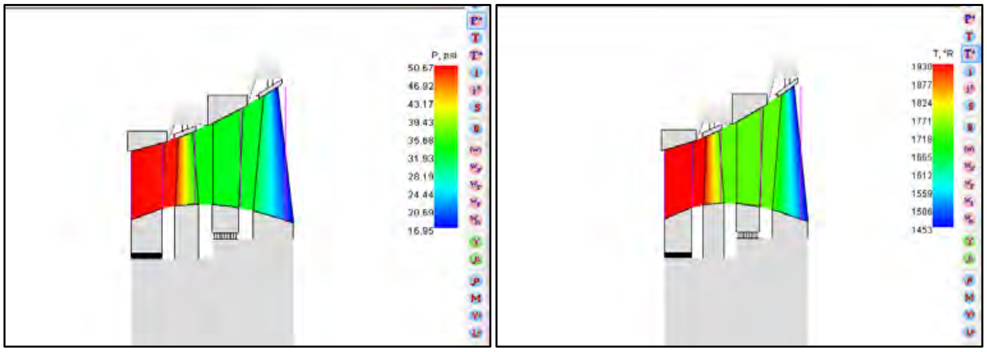

(c) (f)

Figure 35: *Variation of (a) Absolute Mach number, (b) Relative total temperature, (c) Total pressure, (d) Relative Mach number, (e) Relative total pressure, (f) Total temperature, throughout the LPT*

Enthalpy-Entropy curve: There was no sudden velocity or pressure rise throughout the turbines. Fluctuations in entropy and pressure contours were minimized, as a result of which, noise was reduced [29].

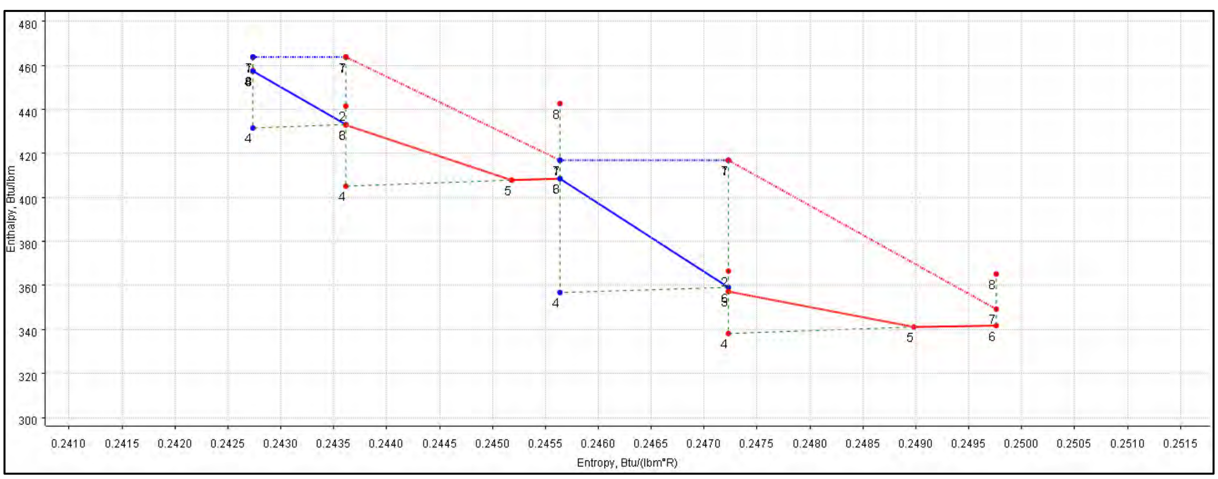

Figure 36: *Enthalpy-entropy curve of LPT*

6.2.2.1 Velocity Triangles

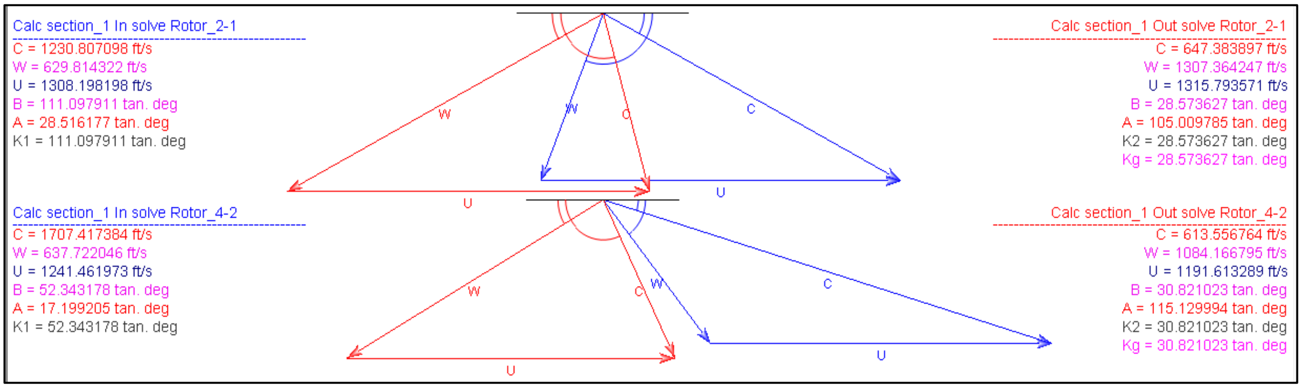

Figure 37: *Velocity triangles at LPT hub*

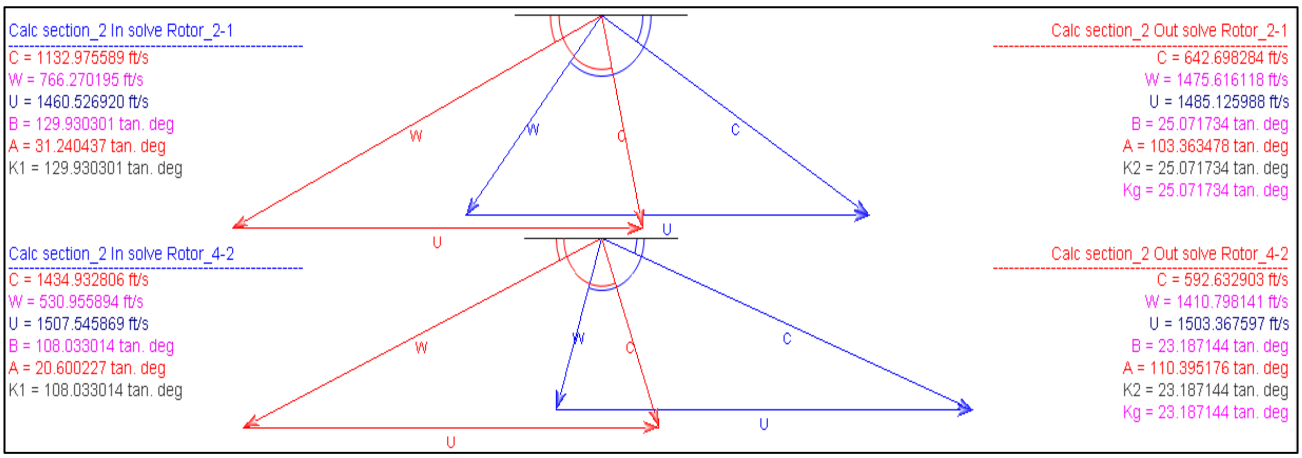

Figure 38: *Velocity triangles at LPT mean line.*

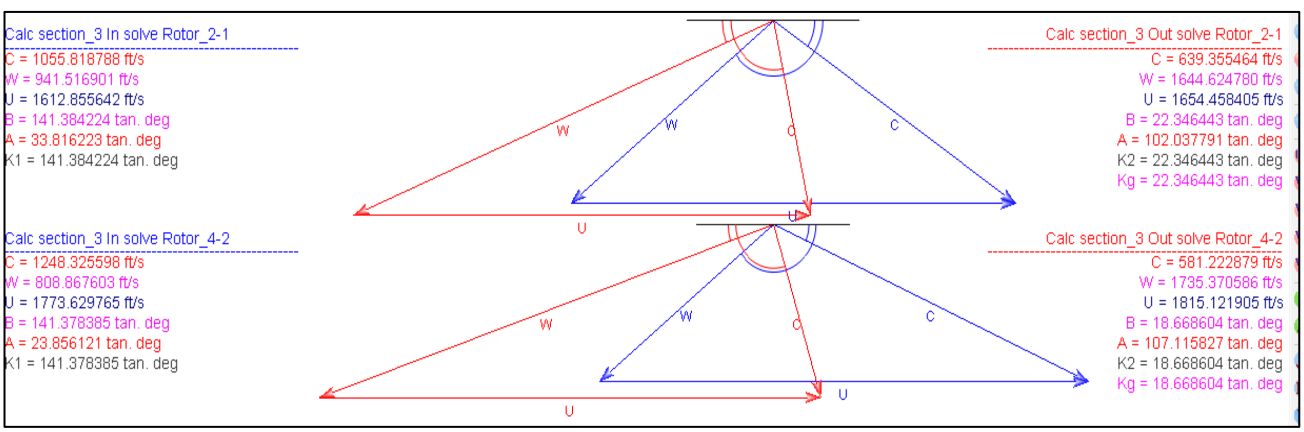

Figure 39: *Velocity triangles at LPT tip*

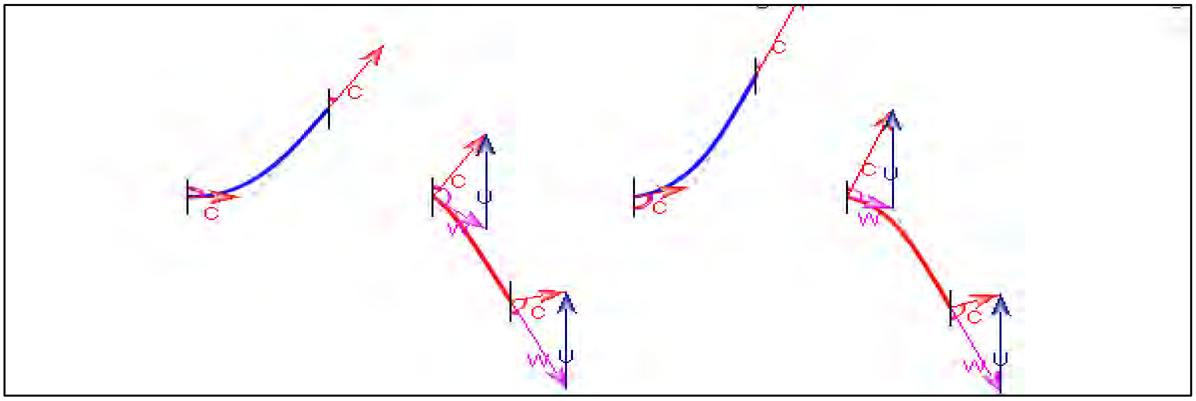

(a)

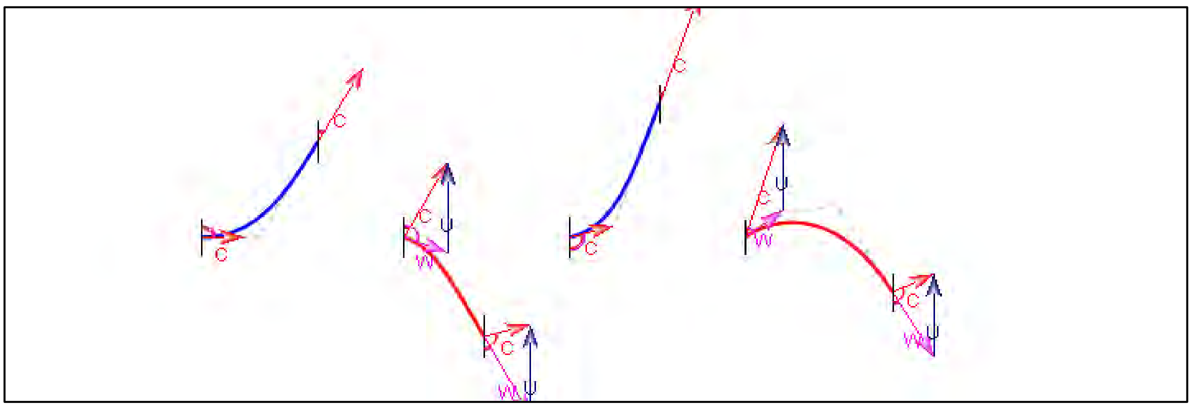

(b)

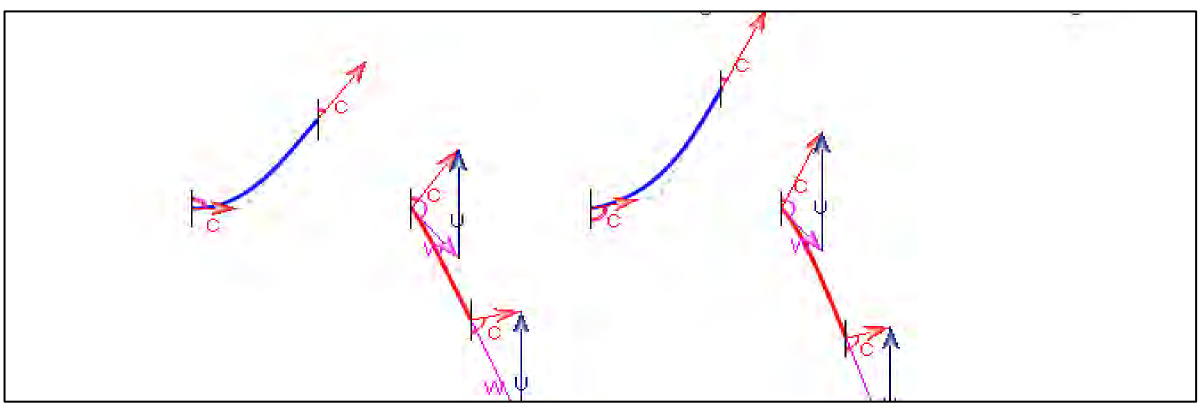

(c)

Figure 40: *Velocity view at stators and rotors of LPT at a) hub, b) mean and c) tip*

6.2.3 Blade Profiling

Blade design for turbines has been done in a similar way as that of compressors. The values of angles and velocities have been taken from AxStream and some parameters were given their typical value. Zweifel's methodology has been used as a calculation criterion and loading factor (Ψ=0.8) has been used in our design. The nozzle factor has its typical value, 0.05.

Table 27: *Stage-wise blade design parameters for turbines*

Parameters	HPT Stage 1	LPT Stage 1	LPT Stage 2
Blade inlet angle	115.04	111.09	52.34
Blade outlet angle	13.45	28.57	30.82
Air inlet angle	115.04	111.09	52.34
Air outlet angle	14.29	28.57	30.82
Stagger angle	64.245	69.83	41.58
Axial chord	0.298	0.297	0.227
Blade chord	0.331	0.317	0.342
Number of blades	102	86	84
Number of stators	85	72	70
DOR	0.696	0.535	0.442
Solidity	0.983	0.767	0.777
Taper ratio	0.8	0.8	0.8
Pitch	0.337	0.413	0.441
Zweifel loading coefficient	0.877	1.432	1.805
Nozzle loss coefficient	0.05	0.05	0.05

6.2.4 Turbine Blade Materials

Turbine blades are put through extremely high rotational and bending stresses. Selection of turbine materials must be done cautiously considering these factors along with high turbine inlet temperatures.

Major effects that take place in turbines are as follows:

Table 28: *Problems caused by different processes*

Effect	**Oxidation**	**Hot corrosion**	**Inter-diffusion**	**Thermal Fatigue**
Extend of damage caused	Severe	Moderate	Severe	Severe

To ensure that the metal or alloy is appropriate, the following key factors should be taken into account:

- High stiffness and tensile strength to ensure accurate blade location and resistance to over-speed burst failure.
- High fatigue strength and resistance to crack propagation to prevent crack initiation and subsequent growth during repeated engine cycling.
- Creep strength to avoid distortion and growth at high temperature regions of the disc.
- Resistance to high temperature oxidation and hot corrosion attack and the ability to withstand fretting damage at mechanical fixings. [30]

Table 29: *Trade-off between different materials which are in use or are expected to be used in the future. [30] [31] [32]*

Material	**Max. Temperature**	**Advantages**	**Density**
Nickel super alloy-718	2619.67ºR	• Highly resistant to sulfide and chloride Stress corrosion cracking • High strength in the aged condition • Good corrosion resistant	0.297 lb/in^3
Cobalt based super alloy	1242.27ºR	• Higher melting points than simple nickel (or iron) alloys • Superior hot corrosion resistance to gas turbine atmospheres due to its high chromium content	0.292 to 0.310 lb/in^3
Nickel super alloy- 706	2939.67ºR	• Easy to machine • Good strength	0.291 lb/in^3
Titanium Based super alloys (TIMETAL 1100)	1571.67ºR	• Good weldability • Good strength for a wide range of temperature	0.164 lb/in^3
Silicon Nitride	2651.67ºR	• Light weight • High melting point • High creep strength	0.124 lb/in^3
Si-C-based ceramic matrix composites	3011.67ºR	• Range of high temperatures and exhibit very high mechanical strength. • Excellent chemical resistance and stiffness-to-weight ratio	0.116 lb/in^3
Carbon Nano tubes	4091.67ºR to 7691.67ºR	• Is very light in weight • High thermal conductivity • Can withstand high pressure and temperature conditions	0.057 lb/in^3

After taking into account all the trade-off criteria, it was concluded that Si-C based ceramic matrix composites most suit the necessary requirements. Silicon carbides can withstand around 1400°C along with good corrosion resistance. Such a high temperature resistance eliminates the need of using a cooling system. Silicon carbide generally does not contain glassy phases at grain boundaries, even when doped sintering additives such as alumina. Due to this rigid interface, the strength is not degraded at very high temperatures [30].

Carbon Nano tubes would theoretically be the best solution for the material to be used as the maximum temperature it can bear is very high as shown in the above table. It is also very light in weight and has a thermal conductivity thrice as much as normal steel and twice as that as that of the Inconel 718. They can remain stable at high temperatures with high tensile strength [32]. But as the current research being conducted in the material does not show any signs of aerospace application by the year 2025, this material was eliminated.

Coatings: As seen in Table 28, one of the reasons why the turbine blades are severely degraded is due to oxidation. To prevent this, a coating similar to the compressor blade coating technique as mentioned in section 6.1.7 is implemented.

6.2.5 Stress Analysis

The governing equation for centrifugal stress in blades is based on material density, rotational speed and blade design. Turbines are highly susceptible towards resonance via vibrations. Therefore, along with stress analysis of turbine, it is crucial to take into account, the resonance by the means of Campbell diagram which are used to analyze the shaft speed in RPM and determine vibration frequencies.

For the calculation of centrifugal stresses, area ratios were taken from AxStream and other design parameters are found using AN^2 rule.

Table 30: *Design parameters for Stress analysis for turbines*

Design Parameters	HPT	LPT
Allowable centrifugal stress, σ_{all} (psi)	40000	40000
Material density (lbm/in^3)	0.0723	0.0723
Taper ratio	0.8	0.8
Angular speed ω (rpm)	30000	30000
Flow Area, A (in^2)	80.284	51.296
Design Centrifugal Stress, σ_c (psi)	32906.4	21024.9
Safety factor	1.215	1.902

The margin of safety in HPT and LPT is 1.215 and 1.9 respectively, which concludes that the design of HPT and LPT rotor blades is safe.

6.3 Stall

An aircraft generally works without any disruptions at design conditions. But when it is operating in off-design conditions, certain conditions like air flow rate, angle of attack etc. change the values of some parameters, thereby decreasing the efficiency of the engine and at times resulting in failure.

The conditions at which stall might occur are as follows

- During takeoffs
- During landing
- Sudden change of flight trajectory
- Sudden acceleration
- Bird strike

When the aircraft is taking off or changing its flight trajectory suddenly, there is a change in angle of attack which results in uneven rise in pressure and entropy contours on some parts of the compressor blades. At times it even results in the reverse flow of the working medium. In order to tackle this challenge of stalling, the fundamental approach is to adjust the angle of attack accordingly.

This can be done either by hub treatment method or using variable stator vanes.

6.3.1 Hub Treatment Method

In this method, the vanes of the stator are casted along with the hub. It is not a very efficient method for low stagger stator rows. There is a significant change in peak static pressure rise on the stator vanes.

But this method involves complex blade designs and the change in the stall onset point and the pressure value is not worth the complexity [33].

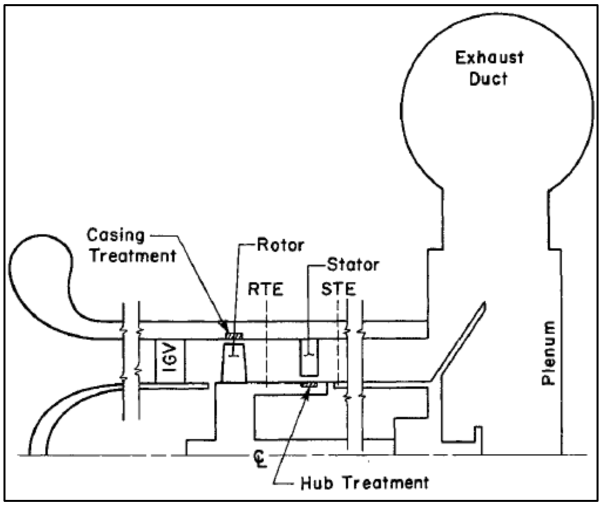

Figure 41: *Schematic of hub treatment method [33].*

6.3.2 Variable Stator Vanes

The stator vanes compress the air and also direct the air to the rotor of the next stage in order to maintain the perfect angle of attack. But during lift offs or landing, the angle of attack changes. This decreases the pressure ratio. In order to maintain that, stator blades are provided with bores at the end, and are connected to the shaft which helps them to rotate [34].

A schedule of the stator has to be prepared in order to cope with pressure ratio across a stage and hence the efficiency of the compressor. The rotation of the stator can be controlled by an actuator system which helps them to reposition according to the schedule [34].

ALTAIR uses variable stator vanes for 1st and 2nd stage operated using a single actuator, as the airflow after that can be maintained once the desired angle of attack is obtained. Studies were also conducted using GasTurb 12 to analyze compressor performance parameters against vane angles during off design conditions.

6.4 Surge

To control the compressor surge margin, an appropriate automatic handling bleed was implemented using GasTurb 12. By doing so, the operating line of the compressor was lowered thereby avoiding a surge.

7. Combustion Chamber

ALTAIR uses a reverse flow annular combustion chamber owing to the current combustor used in the baseline engine. In addition to the existing design, a variable geometry is implemented which leads to over 25% increase of total temperature at combustor outlet and an additional 40% NOx and 50% CO emission reductions [35].

This method is being currently employed for miniature gas turbine engines. The future development of such technology to enable efficient compatibility with turboprop engines is vast considering the fact that this development can improve the optimization of engine operation. The compatibility issues are expected to be solved by 2025 to ensure effective engine operation.

In [35], an experimental research was conducted on a modified version of GTM-120 which is a miniature gas turbine mainly used as a UAV propulsion system. The idea implemented involves a rotating collar with dilution hole pattern located outside the outer liner in the aft portion of the combustor (Figure 42).

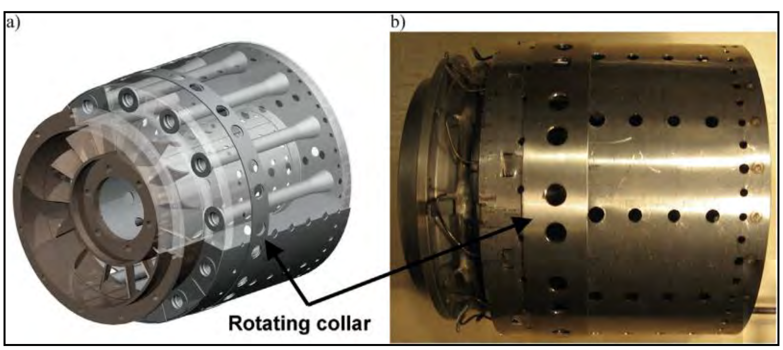

Figure 42: *Variable combustion chamber [35]*

The above stated UAV engine makes use of a quasi-reversed flow combustion process whose working is represented in Figure 43.

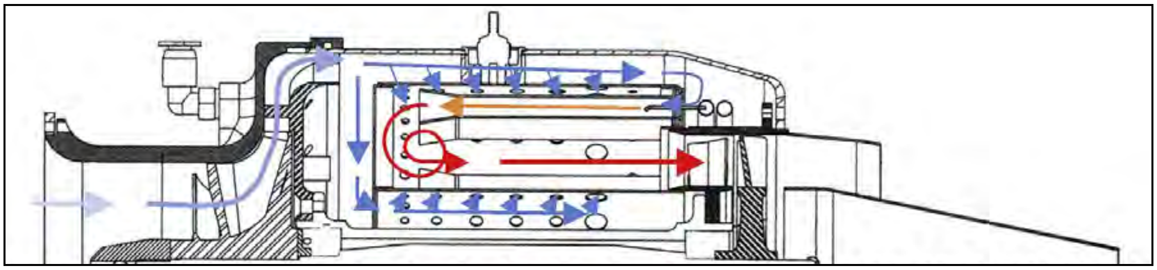

Figure 43: *Quasi-reversed flow of GTM-120 miniature gas turbine combustion chamber [35]*

According to the results of the above conducted experiment it was observed that this particular design of the combustion chamber is optimized to work with maximum efficiency at a particular point which occurs at 80,000 rpm. At this particular rpm the thermal efficiency of the engine is maximum and the corresponding NOx/CO emissions are minimum. Based on certain calculations it was found that the shaft rotation speed of ALTAIR was much less than the optimum shaft rotation speed of the above given design. To overcome this limitation, the above design can be optimized to suit the engine requirements.

7.1 Combustor Pre-diffuser

Considering the outlet Mach number of ALTAIR's compressor section, a pre-diffuser is employed to reduce this number to 0.2 for an optimum combustion process. To shorten the axial length of a combustor pre-diffuser, a dump diffuser is used [13].

The dump diffuser ensures a reduction in the inlet velocity by a magnitude of 0.6 times the original inlet velocity. The major limitation of the use of dump diffuser is the pressure loss of a magnitude of 50% on account of sudden expansion which is compensated by the savings in length and weight as illustrated in [37].

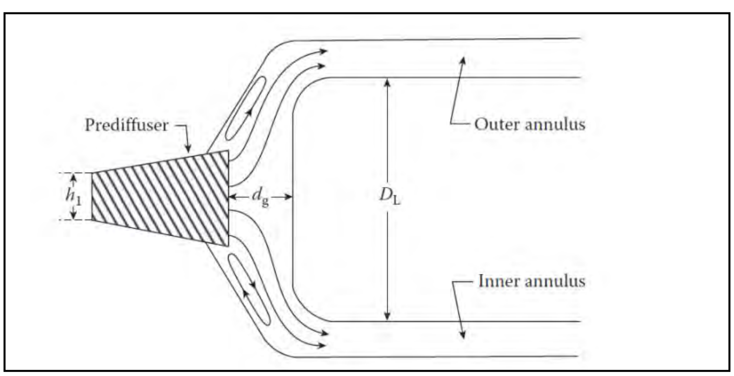

Figure 44: *Dump diffuser [37]*

As stated in [38], the use of lean combustion helps in reducing the NOx emissions to a major extent. On the contrary, the use of this method brings about a disruption in the flow distribution in the combustion chamber and also a reduction in the cooling flow that can be directed. To utilize the above method of combustion it is not only important to optimize the design but also ensure its easy integration.

Experimental results provided in [38] prove the enhanced external aerodynamic performance of a combustor using an integrated OGV/Pre-diffuser design technique. This design involves a modified OGV blade shape produces a secondary wake structure that enables the pre-diffuser to operate at a higher area ratio without any boundary layer separation. Using such a configuration provides a relatively better stable region than a conventional datum design as shown in Figure 45.

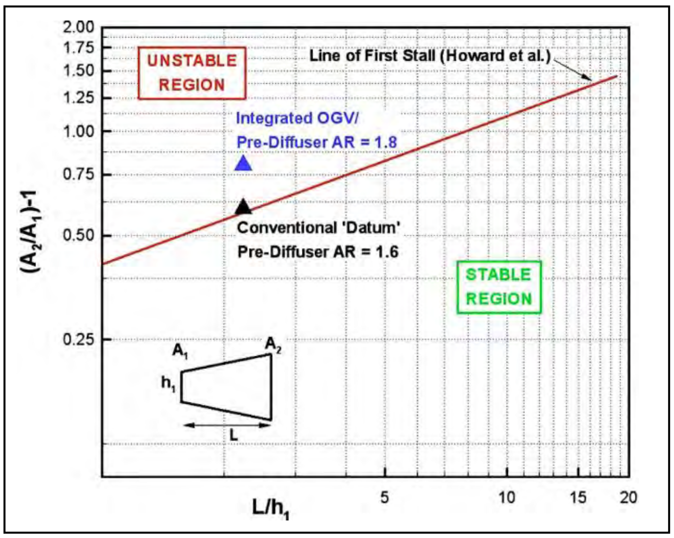

Figure 45: *Datum and integrated geometries on a diffuser chart [38]*

This study was made as an extension of EU project entitled "LOPOCOTEP" (LOw POllutant COmbustor TEchnology Programme) that conducted a detailed experimental and computational study comparing the performance of a conventional OGV/diffuser design [39]. Their analysis reported the following major improvements:

- Increase in the diffuser area ratio from 1.6 to 1.8
- Increase in static pressure recovery with respect to rotor exit by a margin of 5%
- Inner annuli loss reduction by a margin of 10%
- Outer annuli loss reduction by a margin of 20%

7.2 Fuel

As stated in [40], the aviation sector has agreed to cap its net emissions by 2020 and by the year 2050 is expected to half the emissions as compared to 2005 (318.5 million tons of carbon) assuming sustainable biofuels will be well established.

Kondrteiv cycles and waves of innovation as depicted in Figure 46 predicts that by the year 2025 there will be a tremendous breakthrough in the field of green technology [41].

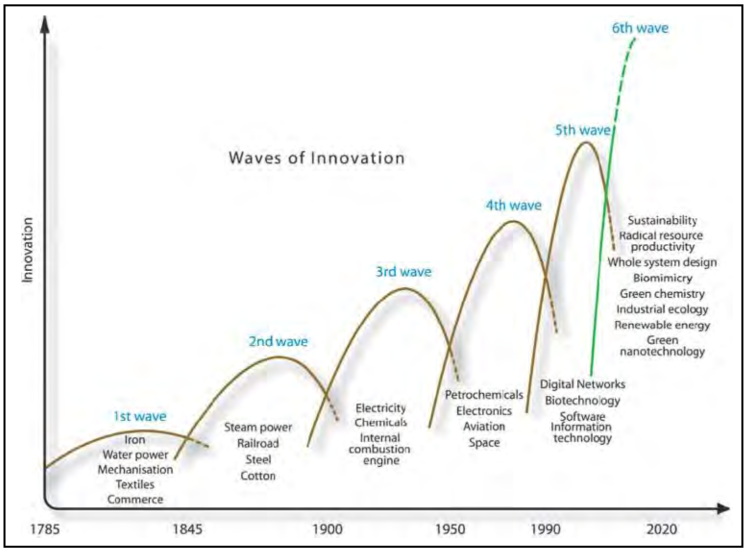

Figure 46: *Kondrteiv cycles and waves of innovation [41]*

The research summarized in [42] shows that green business models are emerging at a very fast rate and that a great understanding is required in order to survive the dynamic environments of the current market taking the case of algae biofuel used for aviation as an example. It was therefore decided that ALTAIR requires a blended aviation fuel or a biofuel in order to outperform all the other engines that would emerge in 2025.

Jet A1 is non-renewable and generates a significant amount of gaseous pollutants. Non-edible low cost vegetable oil such as waste vegetable oil (WVO) and *Jatropha curcas* can be used as feedstock for jet biofuel production as proved in [43].

As stated in [43], several blends of methyl esters prepared by the conversion of Waste oil and *J. curcas* oil through a two-step catalytic reaction with Jet A-1 were prepared and characterized to determine an acceptable ratio in accordance with specifications of jet fuel. The production of this fuel is represented by the flowchart depicted in Figure 47.

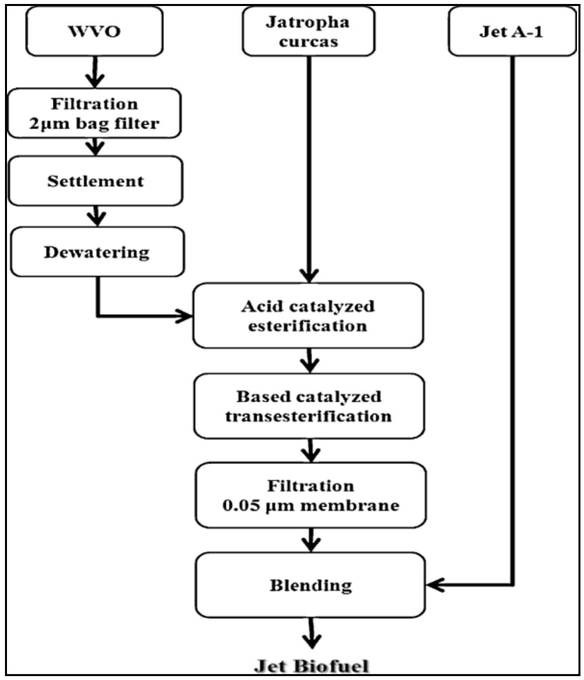

Figure 47: *Flowchart diagram of jet biofuel production [43]*

Blending Jet A1 with methyl esters increases the viscosity of the fuel which results in higher pressure drops, demanding the fuel pump to work harder to retain a constant fuel flow rate. Hence a study was conducted with different binary blend ratios and the results indicated that the binary blends with esters contents of 20% and below have viscosities within the aviation fuel standards as shown in Table 31 [43].

Table 31: *Kinematic viscosity of jet biofuel with different fractions of methyl esters at -40°C [43]*

Jet A-1 (%)	FAME (%)	Kinematic viscosity (mm^2/s)	
		Jatropha oil	Waste vegetable oil
100	0	5.61	5.61
90	10	6.88	6.45
80	20	7.81	7.62
70	30	9.87	9.26
60	40	11.29	11.01
50	50	13.08	12.84
40	60	n.d.*	n.d.*
0	100	n.d.*	n.d.*

The major conclusion drawn from the above study indicates that waste vegetable oil and *J. curcas* can be used as a cheap and non-edible feedstock to produce jet biofuel which will result in the reduction in the use of Kerosene-type Jet A-1 aviation fuel which in turn will help in capping emissions [43].

7.3 Combustion Liner Cooling Technology

To enhance the performance of the combustion chamber and enable it to withstand increasing firing temperatures and contamination a coating must be applied. ALTAIR uses an advanced combustor liner technology based on the following trade off study conducted between the cooling methods mentioned in [44].

Table 32: *Trade-off study between advanced cooling methods [44].*

Angled Multi-hole Effusion Cooling	**Composite Matrix Liner Cooling**
The cooling performance is controlled by a relatively few geometric parameters, namely: sheet thickness, hole size, spacing and plunge angle	The interrupted surface or transpiration cooled concept may be required if the ceramic compliant layer interface is to be maintained at or below 1750°F above which, oxidation of the compliant layer will be a significant problem
Ease of manufacturing and setup	The selection of the ceramic and compliant pad thickness is critical to the success.
Cost effective	Significantly expensive when compared to Angled Multi-hole Effusion Cooling
High relative cooling requirement	Low relative cooling requirement

Although Composite Matrix Liner Cooling appears to be more effective, ALTAIR uses an Angled Multi-hole Effusion Cooling method considering the lack of necessity for tremendous temperature rise requirements as applicable in high performance turbojets and the already used ceramic material for liners and turbine blades as decided in section 7.4. The former can be chosen however if the manufacturing technology is improved and cost cutting methods implemented to install the cooling method.

This cooling method can be optimized by adjusting the effusion geometry and shape of the hole. For example, in the experiments reported in [44] on TF41 combustor liner, decreasing the hole angle from 45° to 20° reduced the cooling requirements by 35%.

7.4 Liner Material Selection

Ceramic Matrix Composites (CMC's) have been receiving a lot of attention lately and are being constantly developed in accordance to the rising demand for high temperature applications. Current developments are being made to enable "ultra-high temperature" applications (around 1650°C) as per [45].These materials facilitate significant gains in efficiency with reduced requirements for cooling along with weight reduction of components [45].

Combustor liner components that have undergone extreme temperature and pressure conditions in a combustion testing rig [47] proved that MI-CMC (Melt Infiltrated Ceramic Matrix Composites) can outperform metallic components like HS-188 which failed after 50 thermal trip cycles as compared to the 200 thermal trip cycles experienced by MI-CMC. Subsequent tests carried out by [46] revealed excellent properties of MI-CMC's.

MI-CMCs are composed of continuous SiC reinforcing fibers in a matrix of SiC+Si. Extensive research conducted by NASA Glenn Institute to implement a 2700°F CMC technology has met with great success and the implementation of this technology would decrease the fuel burn by 6% [48].

NASA's patented technology presents ways to enhance the thermo structural performance of SiC CMC. This can be done so by the production of a protective in-situ grown boron-nitride (iBN) coating on the fibers. This converted fiber is called a “Sylramic-iBN" fiber. These fibers display high creep resistance and exceptional creep-rupture resistance of any commercial SiC fiber till date [49].

Taking all the above points into consideration, ALTAIR will be using a SiC Fiber Reinforced SiC Ceramic Matrix Composite as its liner material.

7.5 Fuel Injection System

The Injector: ALTAIR uses an air blast atomizer. This was decided based on the trade-off study conducted between air blast atomizers over dual-orifice pressure atomizers and air-assist atomizer.

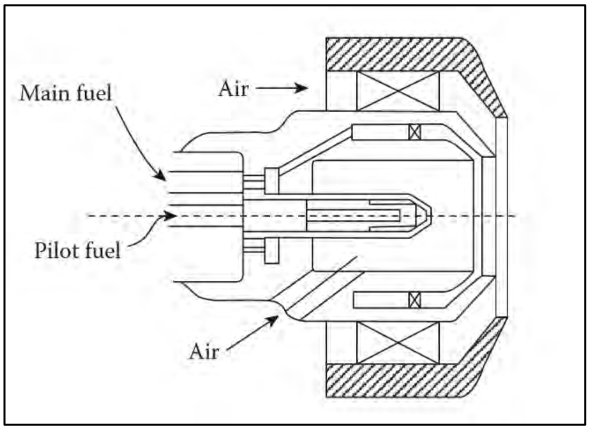

Figure 48: *Representation of the air blast atomizer [37].*

Piloted Air blast: This injector consists of a pre-filming air blast atomizer with a simplex pressure-swirl nozzle located on its centerline. The aim is to overcome the drawbacks of airblast atomizer which has poor atomization and poor lean out performance. Pilot nozzle supplies all fuel at low loads giving a well-atomized spray, and obtaining efficient combustion at idling and start up. Both airblast and pilot nozzles are used to supply fuel at higher power settings.

The advantages of airblast atomizers over dual-orifice pressure atomizers are better mixing of air and fuel drops prior to combustion [37].

The main difference between the air-assist atomizer and airblast atomizers lies in the quantity of air employed and its atomizing velocity.

An important design choice is whether the two swirling airstreams should be counter rotating or co-rotating. A combination of co-rotating inner airstream and counter-rotating outer airstream with respect to the rotational direction of the liquid film, yields the lowest SMD (D_{32}), as compared with other swirler configurations [37].

Injector module: The use of the above decided atomizer in combination with an injector module helps to improve injector efficiency of the engine. The Lean Direct Injection (LDI) concept developed by the NASA Glenn Research Center as a modern technique for future aircraft gas turbines helps in reducing thermal NOx by minimizing flame temperature. As stated in [50] reducing flame temperature alone will not be sufficient to achieve the steep reduction in NOx targets set for the future gas turbines. To overcome this problem, the Multi-Point LDI scheme was introduced by breaking up a few large fuel injectors into many small fuel injectors to produce several small flame zones. The small multi-zone burning provides shorter burning residence time, resulting in low-NOx formation.

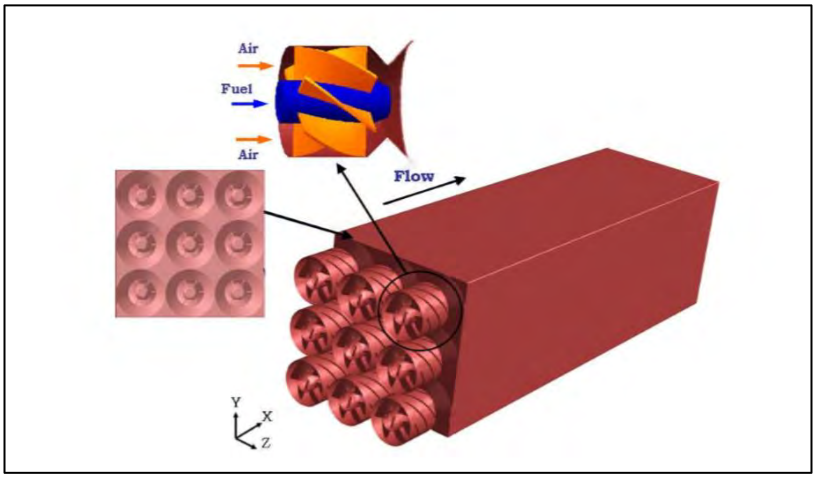

Figure 49: *The MPLDI combustor geometry with the air swirler-fuel injector module [50].*

There is an alternative method that makes use of single element LDI. ALTAIR uses the MPLDI on the basis of given trade-off study between the two existing methods given in Table 33.

The MPLDI configuration comprises of nine swirler-fuel injector modules with a swirl number of 1.23. The center-to-center distance between the modules is 25.4 mm. All the nine swirlers rotate in the same direction. Each air swirler has six helicoidal vanes of 60◦ vane exit angle [50]. The fuel injector is inserted through the center of the swirler and its tip is positioned at the throat of a converging-diverging venturi section which encloses the swirler-fuel injector assembly.

Table 33: *Trade-off study between MPLDI and single element LDI [50].*

Multi Point LDI (MPLDI)	**Single-element LDI**
Smaller drops are obtained	Relatively large drops are obtained
The ranges in which both D10 and D32 vary are small.	The mean diameter ranges are much wider.
The mean diameter profiles are mostly uniform along the axial and radial directions.	The mean diameter profiles are not smooth. Distinct diameter peaks are observed.

Table 34: *Characteristics of combustion fuel injector.*

Injection Systems	**Subsonic cruise**
Number of fuel injectors	09
Swirler Tip Radius, r_t (in)	0.49
Swirler Hub radius, r_h (in)	0.365
Swirler area, A_{sw} (in^2)	0.366
Swirl Blade angle, a_{sw}	60°
Swirl Number, S	1.23

7.6 Combustor Sizing

The reverse flow combustor system is selected such that the combustor length is sufficient to provide the necessary flame stabilization. The typical values of the length – to – diameter ratio for liner ranges from 3 to 6. Combustor loading is a measure of the difficulty of the combustor design duty. This is determined by Figure 50 from [51].

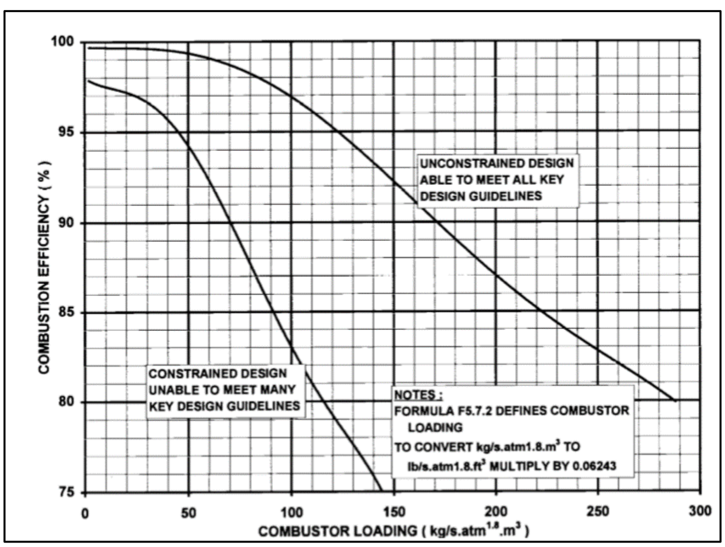

Figure 50: *Combustion efficiency vs Loading [51].*

Similarly, the value of Q is estimated from Table 35 from the Mach number inside the chamber.

Table 35: *Value of Q from Mach Number [51].*

Mach No.	P/PS (–)	(P – PS)/P %	T/TS (–)	$V/\sqrt{T}$ $m/\sqrt{K}\,s$	q $kg\sqrt{K}/m^2\,kPa\,s$	Q $kg\sqrt{K}/m^2\,kPa\,s$
0.01	1.0001	0.0066	1.0000	0.1954	0.6806	0.6806
0.02	1.0003	0.0266	1.0001	0.3908	1.3613	1.3609
0.03	1.0006	0.0598	1.0001	0.5862	2.0420	2.0408
0.04	1.0011	0.1063	1.0003	0.7815	2.7229	2.7200
0.05	1.0017	0.1661	1.0004	0.9768	3.4038	3.3982
0.06	1.0024	0.2390	1.0006	1.1721	4.0850	4.0752
0.07	1.0033	0.3252	1.0008	1.3673	4.7663	4.7508
0.08	1.0043	0.4245	1.0011	1.5624	5.4479	5.4248
0.09	1.0054	0.5368	1.0013	1.7575	6.1297	6.0968
0.10	1.0067	0.6622	1.0017	1.9525	6.8119	6.7668
0.11	1.0081	0.8006	1.0020	2.1473	7.4944	7.4344
0.12	1.0096	0.9519	1.0024	2.3421	8.1772	8.0994
0.13	1.0113	1.1160	1.0028	2.5368	8.8605	8.7616
0.14	1.0131	1.2929	1.0032	2.7313	9.5442	9.4208
0.15	1.0150	1.4824	1.0037	2.9257	10.2283	10.0767
0.16	1.0171	1.6845	1.0042	3.1199	10.9130	10.7292
0.17	1.0194	1.8990	1.0048	3.3140	11.5982	11.3780
0.18	1.0217	2.1259	1.0053	3.5080	12.2840	12.0228
0.19	1.0242	2.3651	1.0060	3.7017	12.9704	12.6636
0.20	1.0269	2.6164	1.0066	3.8953	13.6574	13.3001
0.21	1.0297	2.8798	1.0073	4.0887	14.3451	13.9320

Table 36 illustrates the estimated parameters for combustion chamber. The parameters have been calculated from [51].

Table 36: *Combustion Chamber Parameters*

Parameters	**Values**
Air mass flow rate (lbm/s)*	9.84
Inlet pressure (psi)*	170.454
Inlet temperature (K)*	344.161
Combustor Average MN	0.2
Efficiency	0.9
F/A ratio*	0.069
Combustor loading	35
Intensity ($MW/atm.m^3$)	170.438
$W_{primary}$ (lbm/s) *	3.03
Primary zone exit temperature (K)	2600
L/D	3.5
A_{can} (in^2)	9.08
Combustor diameter (in)	3.58
Combustor length (in)	12.53
ER of primary zone	1.02
Velocity of flame (m/s)	199.485
Residence time (ms)	0.15955

**from GasTurb 12 solution for optimized engine*

8. Exhaust

ALTAIR utilizes the same exhaust system as used in the baseline engine.

It consists of

Exhaust Duct: A heat-resistant divergent duct with an outlet port on each side of the case.Apart from providing an outer gas path, this duct also provides structural support to the reduction gearbox [52].

Exhaust Stack: It is a bent pipe through which combustion product gases are released to the atmosphere.

9. Engine Weight

Following the technique of statistical weight analysis outlined in [9], the preliminary weight estimate is obtained. This technique utilizes regression analysis of rated SHP and Engine weight for various turboprop engines weights to estimate weight on the basis of rated SHP.

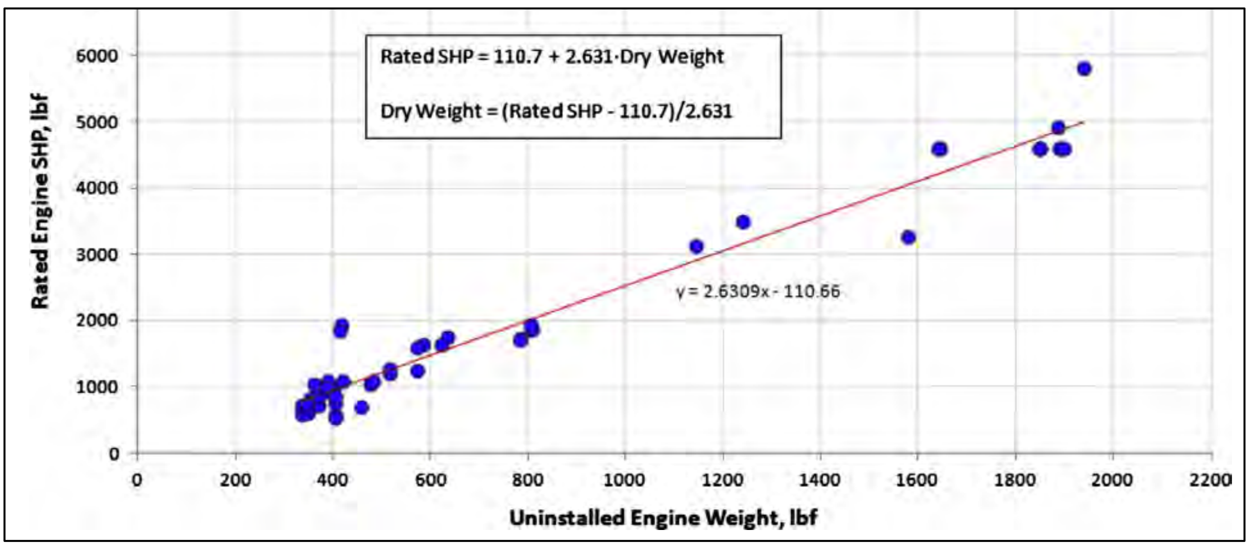

Figure 51: *Correlation between the uninstalled weight of turboprops and Rated Power [9].*

Based on the following published manufacturer's data the following equation is obtained to calculate Engine Weight

$$W_{ENG} = \frac{P_{rated} - 110.7}{2.631}$$

Using this the preliminary weight of ALTAIR engine is obtained as
$W_{ENG} =$ 584.48 lbm.

This estimate was close to the weight of the engine with a rated power of approximately 1650 shp obtained from GasTurb 12 while considering the optimized engine cycle with the same materials used in the baseline.

In this technique an overall analysis is performed. Many component based weight analysis programs like WATE++, Sagerser et al method are available for improved results. GasTurb 12has a component based engine weight estimation module which is used to find the weight of ALTAIR.

The Preliminary weight obtained is high as the statistical estimation considers the weight of the engine with respect to the conventional materials.

The weight of ALTAIR, however, was computed in accordance to the emerging technologies for weight reduction as stated in [53]. The suggested estimates for utilizing advanced materials were composed by modifying the WATE++ code (A computer code for gas turbine engine weight estimation developed by NASA).

The following materials suggested in [53] have been considered for use in ALTAIR.

Table 37: *Technologies for weight reduction [53]*

Component	Current Technology	Future Technology	Weight Reduction Potential (% of Baseline)	References	Challenges
Shafts	Steel Alloys	Metal Matrix Composites	30% compared to current designs	MTU: Steffens and Wihelm	
Fan Blades	Composite, Titanium	More incorporation of more PMC	40%-45% improvement over Ti forging	MTU: Steffens and Wihelm	FOD, Erosion, Quality Control
Fan Containment	Alloy, Emerging Composite	Composite/Kevlar	30% over alloy hardware	NASA CR-2005-213969	Definition of prime reliable components
Compressor Blades	Titanium, Nickel alloy rear stages, IBR or "blisk" construction	Titanium Aluminide components	30-40% weight reduction current Ti components	MTU: Smarsly 2006 revised from P&W communication	
Compressor Disk	Titanium, Nickel alloy rear stages	Titanium Matrix Composite Rings	20-30% over titanium disks	MTU: Smarsly 2008	Production Cost, Quality Assurance
HPT Blades	Nickel Alloy	CMC	30-40% compared to nickel alloys	P&W communication	Cooling the blades, FOD, creep, matrix fiber reactions
HPT Disk	Nickel Alloy	CMC	30-40% compared to nickel alloys	Pratt recommendation	Disk fracture, creep, matrix-fiber reactions
LPT Blades	Nickel Alloy, Present Day Stage Loading	50% stage loading increase, TiAl or CMC components	30% due to stage loading (non additive) 30% due to TiAl or CMC	ASME GT2003-38374 MTU: Steffens and Wihelm	Maintaining efficiency at higher loading, creep, matrix-fiber reactions
LPT Disk	Nickel Alloy	50% stage loading increase, TiAl or CMC components	30% due to stage loading (non additive) 30% due to TiAl or CMC	ASME GT2003-38374 MTU: Steffens and Wihelm	Creep, matrix-fiber reactions
Fan Drive Gearbox	Baseline	improved materials	25% according to NASA trend P&W suggests 10-15%	NASA/TM-2005-213800 P&W communication	Reliability in the presence of corrosive oil environment
Major frames	Aluminum, Titanium, Nickel	More composites for low temperature, ceramics for higher temperature	20-30% from current designs	P&W communication	
Accessories	Baseline	improved materials	10% over baseline	P&W communication	

The densities of all the materials stated in [53] were used as input data in GasTurb 12 for the optimized cycle used in ALTAIR and the effective engine weight was found out to be 500 lbs (i.e., 12.6% reduction).

10. Bearings

Foil bearings are implemented in ALTAIR over the conventional anti-frictional bearings that are being used currently. This will enable the bearing system to operate at a higher efficiency due to a relatively smaller heat loss as compared to oil bearings coupled with less parasitic drag at these elevated temperatures. These bearings were designed specifically for high speed and high temperature applications and were successfully tested on aircrafts like Boeing 737 during the early 1960s. Other advantages include a quieter operation, a high environmental durability and no scheduled maintenance [54].

ALTAIR uses a "third generation" foil bearing which involves an uncoated super-alloy foil bearing lubricated with PS304, a plasma sprayed composite solid lubricant. This lubricant acts as a thin foil coating layer during high temperature operations thereby enhancing its life to about 100,000 start/stop cycles at around 650°C [55]. Its performance is indicated in Figure 52.

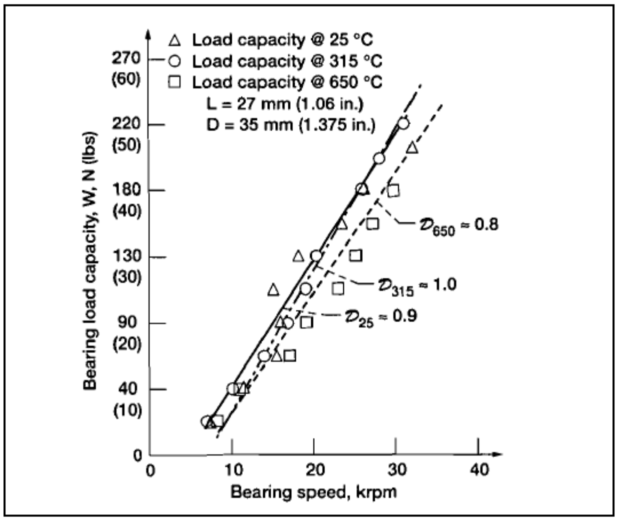

Figure 52: *Foil bearing load capacity for third generation bump foil bearing operating against PS304 coated shaft form 25°C to 650°C [56]*

To ensure the stability of the bearing system at high speed applications and provide an adequate stiffness, staggered bumps are employed in the bearing [57] as shown in Figure 53.

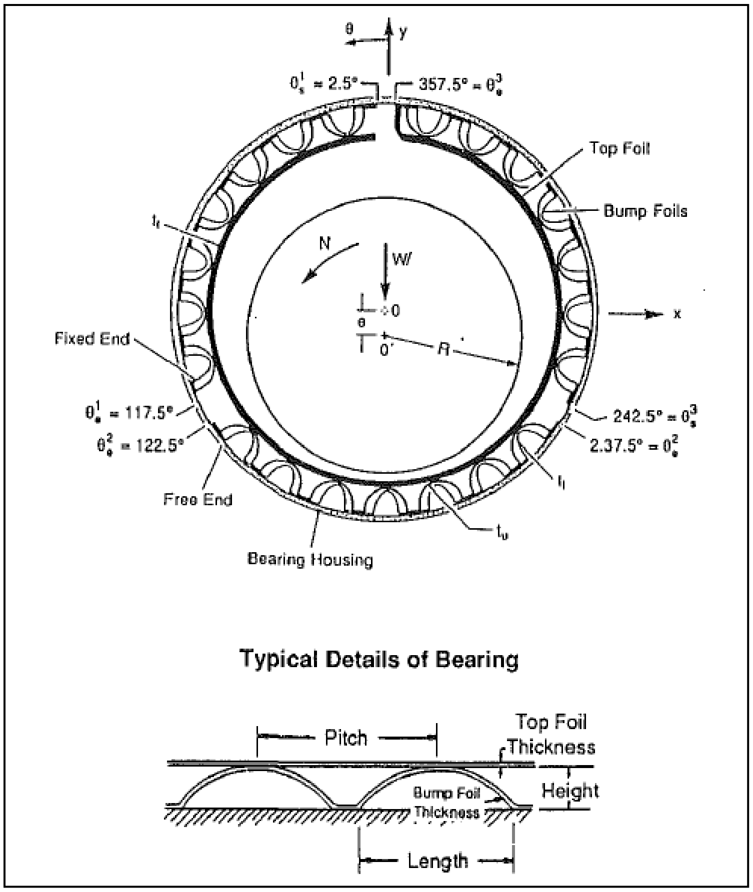

***Figure 53:** Foil bearing design [57]*

Such a bearing design has a capability of reaching around 132,000 rpm and a load capacity of 163.6 lbs [57] which is well above the configurations associated with the design point of ALTAIR.

11. Integrated Propulsion System

It is clearly evident that constant developments are being made in the R&D sector of the aerospace industry to improve the fuel efficiency and reduce the overall weight as much as possible. The search for supremacy is never ending and ALTAIR must inculcate a more sophisticated and automated technology and also preserve the safety of the aircraft and everything aboard in order to withstand the emerging technologies in 2025.

One such technology which is very likely implementable by the year 2025 is the Integrated Flight Propulsion System (IFPS). This technology involves the idea of combining the control power of vectoring and reversing nozzles and aerodynamic surfaces of the aircraft to enhance the performance of the engine [58].

The Pratt & Whitney and Northrop companies together, under the Air Force Wright Research and Development Center (WRDC) designed and demonstrated INTERFACE II Program which is an advanced IFPS [58]. This program proved that using thrust vectoring and reversing nozzles as primary control surfaces improved the engine performance significantly. It also suggested that extending and developing on the preliminary idea of this program with emerging technology would make it implementable for future aircraft engines.

The results obtained in [59] demonstrates the incorporation of IFPS to improve both performance and safety of an aircraft. By observing the trend in Engine control technology from Hydro Mechanical Engine Control to Electronic Engine Control to Full Authority Digital Electronic Control (FADEC) system, it can be concluded that the future advancements will be inclined towards an automated control system.

Doing so will make sure of preserving numerous command laws and a better comprehension of the data obtained by the engine control system thereby providing a reduced fuel consumption, increased engine thrust and potential improvements in reliability, life cycle cost, weight, and maintenance actions [59].

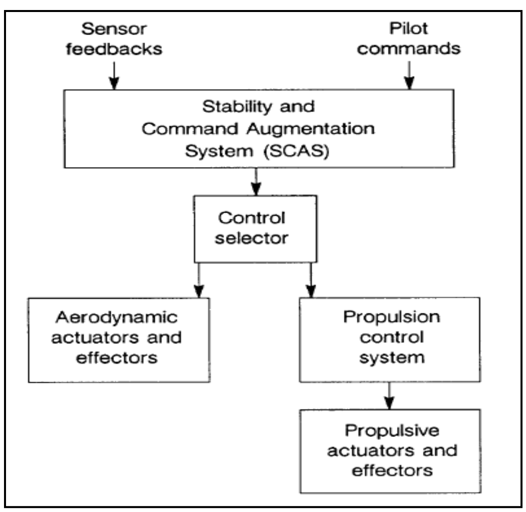

Figure 54: *Control System Functional Overview using INTERFACE II [59]*

Another subsequent study based on the Quadratic Gaussian/Loop Transfer Recovery (LQG/LTR) methodology conducted by NASA [60] on a two spool turbofan engine and equipped with a 2D thrust vectoring nozzle states that the stability robustness of the control system has improved by manifold. Although its implementation might not seem viable on a large scale as of today, we could expect breakthroughs in this technology by 2025.

12. Open Rotor System

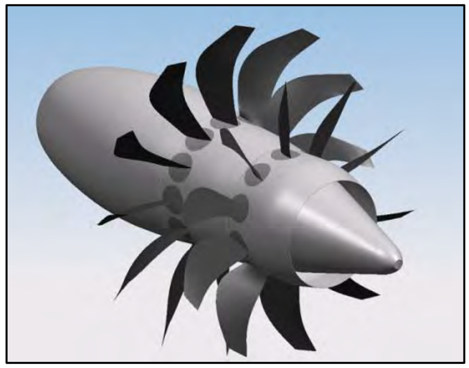

Figure 55: *Open rotor system [61]*

An open rotor system can operate at higher speed than conventional turboprops. It contains set of two propellers or blades which tend to throw air out. The forward blades push the air back whereas the rear ones suck it. The power output from open rotor is equivalent to conventional turboprops having twice the diameter.

The fuel consumption benefit of open rotor propulsion compared to equivalent technology turbofan engines was typically found to be around 25% [62].

Table 38: *Technology goals of NASA for subsonic transport aircraft [62]*

TECHNOLOGY BENEFITS†*	TECHNOLOGY GENERATIONS (Technology Readiness Level = 4-6)		
	N+1 (2015)	N+2 (2020**)	N+3 (2025)
Noise (cum margin rel. to Stage 4)	-32 dB	-42 dB	-71 dB
LTO NOx Emissions (rel. to CAEP 6)	-60%	-75%	-80%
Cruise NOx Emissions (rel. to 2005 best in class)	-55%	-70%	-80%
Aircraft Fuel/Energy Consumption‡ (rel. to 2005 best in class)	-33%	-50%	-60%

Research and Development: Industry and academic groups such as *DREAM* and have taken up the challenge of reducing the noise complication of open rotor engines. Concept designs such as the *EasyJet EcoJet* have been produced and academic studies such as the OMEGA 'Integrated study of advanced open rotor powered aircraft' are underway. The detailed research and development work into open rotor engines will be undertaken by engine manufacturers, through research and technology validation programs such as DREAM and the CLEAN SKY Joint Technology Initiative, both commenced in 2008 [63].

*EasyJe*t predicts that the *EcoJet*, which is to be powered by open rotor engines the potential to deliver CO2 and NOx emission reductions of 50% and 75% respectively, and a 25% reduction in noise, compared to current Boeing 737 and Airbus A320 variants.

DREAM is a research and development program that aims to demonstrate new open rotor engine concepts. Led by Rolls-Royce and involving 47 partners, it is hoped that engines developed and validated in the project will achieve a 27% reduction in CO2 emissions and a 3-decibel reduction in noise per operating point relative to year 2000 engines [63].

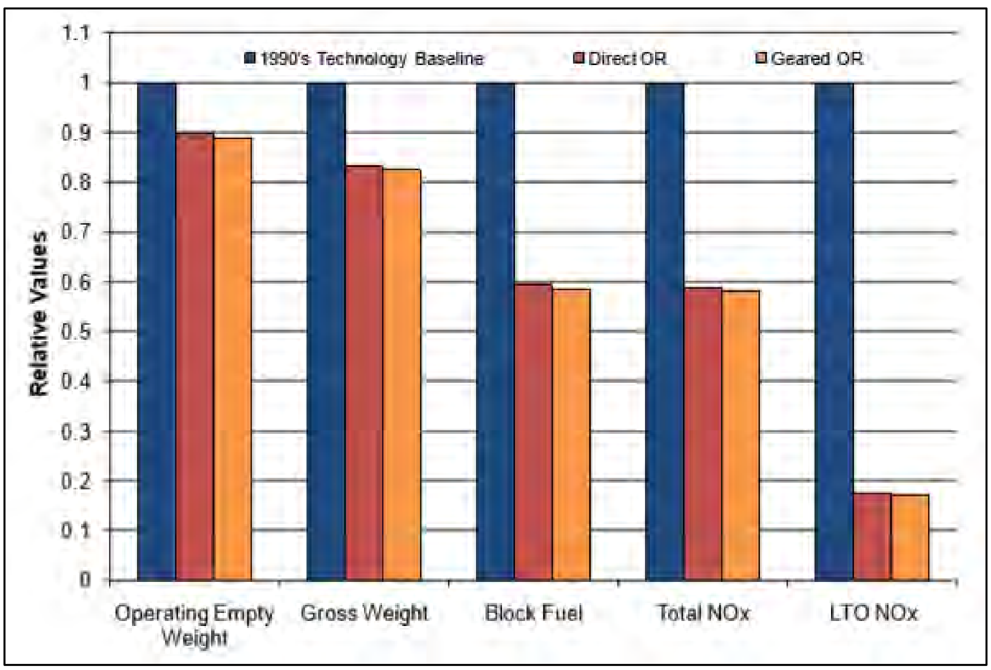

Figure 56: *Advanced open rotor vehicle weight, fuel and emissions relative to 1990s technology baseline [62]*

13. CAD Model

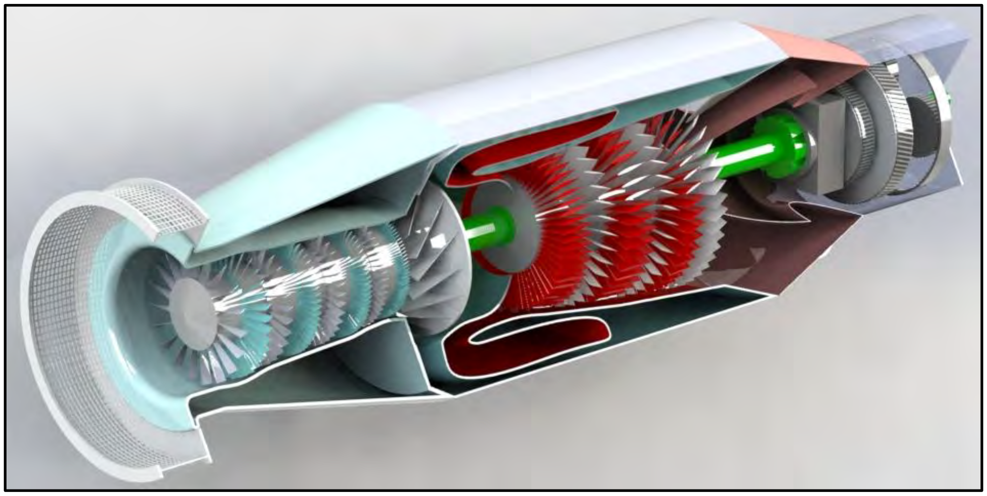

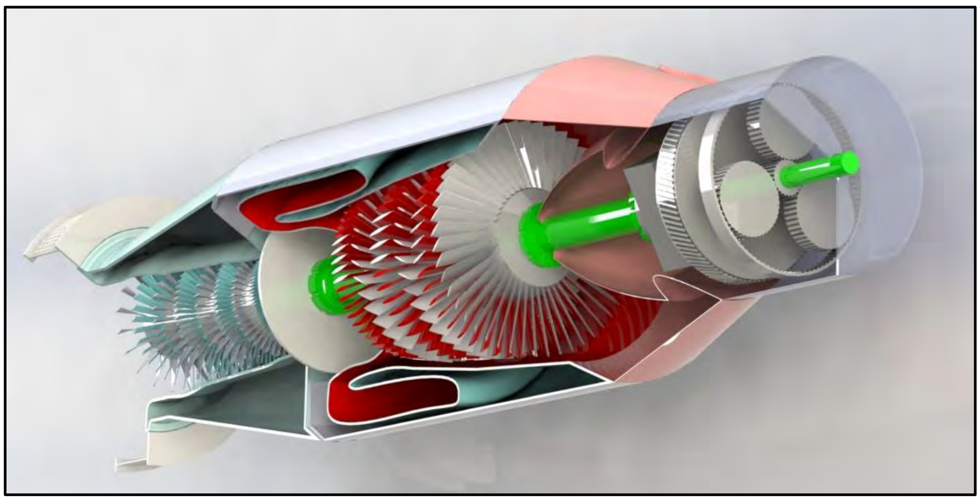

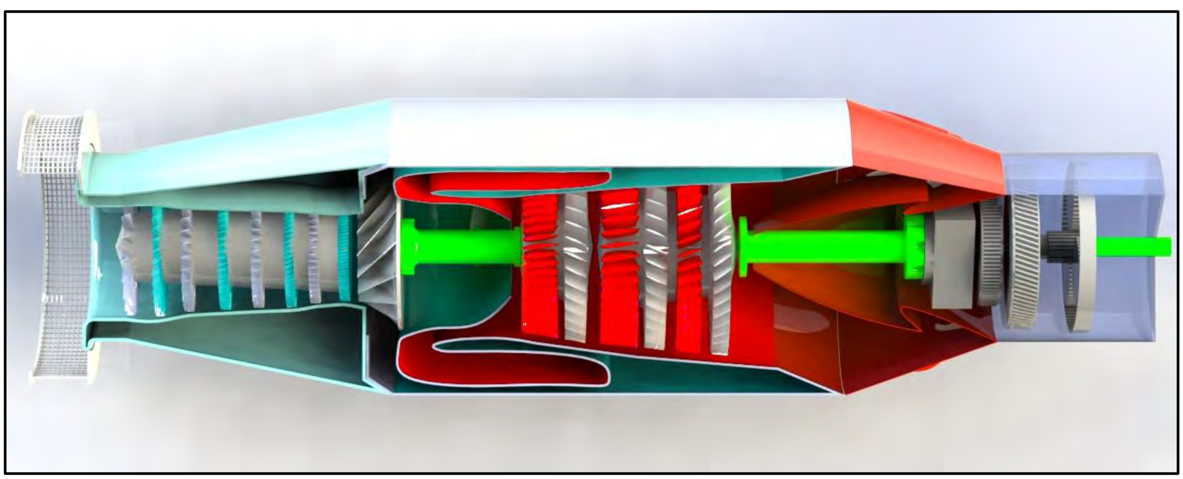

CAD model designed using SolidWorks 2013

REFERENCES:

1. Anon, “Candidate Engines for a Next Generation Single-Engine Turboprop Aircraft”, AIAA Foundation Undergraduate Team Engine Design Competition, 2016.
2. Kurzke, Joachim, “GasTurb 12: A Design & Off-Design Performance Program for GasTurb 12ine,” [http://www.GasTurb.de], GasTurb 12 GmbH, Templergraben 55, 52062Aachen, Germany, 2012.
3. Aircraft Powerplant, Thomas W. Wild and Michael J. Kroes Eight Edition
4. https://www.easa.europa.eu/system/files/dfu/TCDS%20PW100%20series_IM%20E%20041_Issue%2003_final.pdf
5. http://www.pwc.ca/en/engines/pw100-pw150
6. Taylor, John W.R. F.R Hist S, ARAeS (1962). Jane's All the World's Aircraft 1962-63. London: Sampson, Low, Marston & Co Ltd
7. https://www.easa.europa.eu/system/files/dfu/TCDS.IM_.E.010_issue%2005_20150612_1.0.pdf
8. https://aerocontent.honeywell.com/aero/common/documents/myaerospacecatalog-documents/BA_brochures-documents/Engines-documents/TPE331-14_Turboprop_Engine.pdf
9. General Aviation Aircraft Design: Applied Methods And Procedures, Snorri Gudmundsson
10. 4th Edition, Gas Turbine Theory, H Cohen, Gfc Rogers Professor Emeritus, Hih Saravanamuttoo.
11. Richard Leyes Ii, William Fleming, The History Of North American Small Gas Turbine Aircraft Engines, 1999
12. Aircraft Engine Design Second Edition, Jack D. Mattingly, William H. Heiser, David T. Pratt.
13. Aircraft Propulsion, Second Edition, Saeed Farokhi, Phd Professor Aerospace Engineering Department The University of Kansas, USA
14. Turboshaft Engine Air Particle Separation, Antonio Filippone & Nicholas Bojdo, The University of Manchester, Manchester M60 1QD, United Kingdom.
15. De-Icing of Aircraft Turbine Engine Inlets, H.A. Rosenthal, D.O. Nelepovitz, H.M. Rockholt, Rohr Industries, Inc. Chula Vista.
16. Airbus patented technology keeps the A380 quiet. http://www.airbus.com/newsevents/news-events-single/detail/airbus-patented-technology-keeps-the-a380-quiet/
17. www.sky-chaser.com/aereng.htm
18. http://medium.com/war-is-boring/
19. Effect of temperature and pressure on stress of impeller in axial-centrifugal combined compressor Xinqian Zheng and Chuang Ding.

20. Review of Efficiency and Stable Operating Range Enhancements Options of Centrifugal Compressors Al-Busaidi Waleed and Pericles Pilidis School of Aerospace, Transport and Manufacturing, Cranfield University, Bedfordshire, UK
21. Deswirler system for centrifugal compressor, US 6279322 B1, Zaher M. Moussa
22. Systematic two-dimensional cascade tests of NACA 65-series compressor blades at low speeds, L. Joseph Herrig, James C. Emery, and John R. Erwin
23. Materials for Gas Turbines – An Overview, Nageswara Rao Muktinutalapati, VIT University, India
24. High cycle fatigue in aircraft gas turbines - an industry perspective B.A. COWLES Materials and Mechanics Engineering, Pratt Whitney, P O. Box 109600, West Palm Beach, Florida 33410-9800, USA
25. http://www.matweb.com/errorUser.aspx?msgid=2&ckck=nocheck
26. Design and Development of Smartcoatings for Gas Turbines.Gurrappa1 and I.V.S. Yashwanth21, Defence Metallurgical Research Laborator, Kanchanbagh PO, Hyderabad-500 058,2M.V.S.R. Engineering College, Nadargul, Hyderabad-501 510, India
27. Advanced Materials for Aircraft Engine Applications Author(s): Daniel G. Backman and James C. Williams Source: Science, New Series, Vol. 255, No. 5048 (Feb. 28, 1992), pp. 1082-1087 Published by: American Association for the Advancement of Science Stable URL: http://www.jstor.org/stable/2876677 Accessed: 20-09-2016 02:36 UTC
28. Thermal barrier coatings technology: critical review, progress update, remaining challenges and prospects, R Darolia, 2013
29. The Interaction of Entropy Fluctuations with Turbine Blade Rows; A Mechanism of Turbojet Engine Noise, N.A. Cumpsty and F.E. Marble, 1976.
30. Gas Turbine Materials- Current status and its Developmental Prospects-A Critical Review, A.Dinesh Kumar, S.Sathyanarayanan, Sayantan Datta Gupta, Dr.M.NageswaraRao
31. Advanced Materials used for different components of Gas Turbine Shailendra Kumar Bohidar, Ravi Dewangan, Prof.Kalpit Kaurase
32. Aircraft Turbine Blades and Expected Advancement in Technology Using Carbon Nanotubes Jitamitra Swain Kumar Gaurav Dheerendra Singh Prakash Kumar Sen Shailendra Kumar Bohidar, Department of Mechanical Engineering Kirodimal Institute of Technology, Raigarh, Chhattisgarh, India
33. Effects of Compressor Hub Treatment on Stator Stall and Pressure Rise, P Cheng, M E PrelUE M Greitzer, J and C S Tan§, Massachusetts Institute of Technology, Cambridge, Massachusetts
34. Variable Stator Vane Mounting and Vane Actuatiqn System for an Axial Flow Compressor of a Gas Turbine Engine Vendatasubbu Eta 415/160
35. Impact of variable geometry combustor on performance and emissions from miniature gas turbine engine Maciej Chmielewski, Marian Gieras

36. M. Chmielewski, M. Gieras, Study of combustion efficiency and pollutant emissions in a miniature gas turbine with the combustion chamber of variable geometry, Rynek Energii 4 (119) (2015)
37. Gas Turbine Combustion: Alternative Fuels and Emissions, Third Edition, Arthur H. Lefebvre and Dilip R. Ballal
38. Enhanced External Aerodynamic Performance of a Generic Combustor Using an Integrated OGV/Prediffuser design technique A. Duncan Walker, Jon F. Carrotte, James J. McGuirk
39. Barker, A. G., Carrotte, J. F., Luff, J., and McGuirk, J. J., 2003, "Design of an Integrated OGV/Diffuser System," Final Report No. TT03R01, for EU FP5 project, GRD1-2000-25062: "LOPOCOTEP."
40. Beginner's Guide to Aviation Efficiency, Air Transport Action Group (ATAG), November 2010
41. Hargroves, K., Smith, M.H. (Eds.), 2005. Innovation and Governance in the 21st Century. Earthscan, London
42. Nair, S., Paulose, H., Emergence of green business models: The case of algae biofuel for aviation. Energy Policy (2013)
43. Blended aviation biofuel from esterified Jatropha curcas and waste vegetable oils, SaeidBaroutian, Mohamed K. Aroua, Abdul Aziz Abdul Raman, Azzahra Shafie , Raja Adeliza Ismail, Hartini Hamdan
44. Advanced Combustor Liner Cooling Technology for Gas Turbines, Aspi R. Wadia, General Electric Company, Cincinnati, Ohio 45215
45. Melt-Infiltrated Refractory Ceramic Matrix Composites, August 1 2014, Tim Stewart, Brian Williams, and Jerry Brockmeyer
46. Rig and Engine Testing of Melt Infiltrated Ceramic Composites for Combustor and Shroud Applications Gregory S. Corman, Anthony J. Dean, Stephen Brabetz, Milivoj K. Brun and Krishan L. Luthra GE Corporate Research and Development Schenectady, NY Leonardo Tognarelli and Mario Pecchioli Nuovo Pignone GE Power Systems Florence, Italy
47. Dean, A., Corman, G., Bagepalli, B., Luthra, K., DiMascio, P., and Orenstein, R., 1999, "Design and Testing of CFCC shroud and Combustor Components," ASME paper 99-GT-235, presented at the 44th ASME Gas Turbine and Aeroengine Technical Congress, Exposition and Users Symposium, June 7- 10, 1999, Indianapolis, IN
48. CMC Technology Advancements for Gas Turbine Engine Applications Joseph E. Grady NASA Glenn Research Center USA
49. Silicon Carbide (SiC) Fiber Reinforced SiC Matrix Composites, Patent No: 7,427,428; 7,687,016; 8,894,918
50. Flow Characteristics in Lean Direct Injection Combustors, Dipanjay, Dewanji
51. Gas Turbine Performance, Second Edition, Philip P. Walsh
52. Descriptive Course and Guide to Troubleshooting, United Turbine Corp

53. N+3 Aircraft Concept Designs and Trade Studies, Final Report ,Volume 2: Appendices—Design Methodologies for Aerodynamics Structures, Weight, and Thermodynamic Cycles, E.M. Greitzer, P.A. Bonnefoy, E. de la Rosa Blanco, C.S. Dorbian, M. Drela, D.K. Hall, R.J. Hansman, J.I. Hileman, R.H. Liebeck, J. Lovegren, P. Mody, J.A. Pertuze, S. Sato, Z.S. Spakovszky, and C.S. Tan Massachusetts Institute of Technology, Cambridge, Massachusetts, J.S. Hollman, J.E. Duda, N. Fitzgerald, J. Houghton, J.L. Kerrebrock, G.F. Kiwada, D. Kordonowy, J.C. Parrish, J. Tylko, and E.A. Wen Aurora Flight Sciences, Cambridge, Massachusetts W.K. Lord, Pratt & Whitney, East Hartford, Connecticut
54. http://www.nasa.gov/centers/glenn/about/fs14grc.html
55. Load Capacity Estimation of Foil Air Journal Bearings for Oil-Free Turbomachinery Applications, C. Dellacorte & M. J. Valco, National Aeronautics and Space Administration, Glenn Research Center, Cleveland, Ohio,44135, U.S. Army Research Laboratory, National Aeronautics and Space Administration, Glenn Research Center, Cleveland, Ohio, 44135, 2008
56. Della Cone, C., "A New Foil Air Bearing Test Rig for Use to 70WC and 70.000 rpm," Trib. Trans., 41, 3, pp 335-340, 1998
57. Advancements in the Performance of Aerodynamic Foil Journal Bearings: High Speed and Load Capability, H. Heshmat, Mechanical Technology Incorporated, 968 Albany-Shaker Rd., Latham, NY 12110
58. Integrated Flight/Propulsion Control for Flight Critical Applications: A Propulsion System Perspective Kenneth D Tillman, Timothy J. Ikeler, Pratt & Whitney, Government Engine Business, West Palm Beach, Florida ASME 1991
59. Integrated flight propulsion control system, Sundararajan, Janakiraman, QuEST Global Services, 2013
60. Integrated Flight/Propulsion Control System Design Based on a Centralized Approach, Sanjay Garg and Duane L. Mattern, Randy E. Bullard, NASA, 1989
61. http://cafe.foundation/blog/page/44/
62. Initial Assessment of Open Rotor Propulsion Applied to an Advanced Single-Aisle Aircraft Mark D. Guynn, Jeffrey J. Berton, Eric S. Hendricks3, Michael T. Tong4, and William J. Haller and Douglas R Thurman.(AIAA 2011-7058)
63. SBAC Aviation and Environment Briefing Papers 3: Open Rotor Engines

APPENDIX A - Gantt Chart

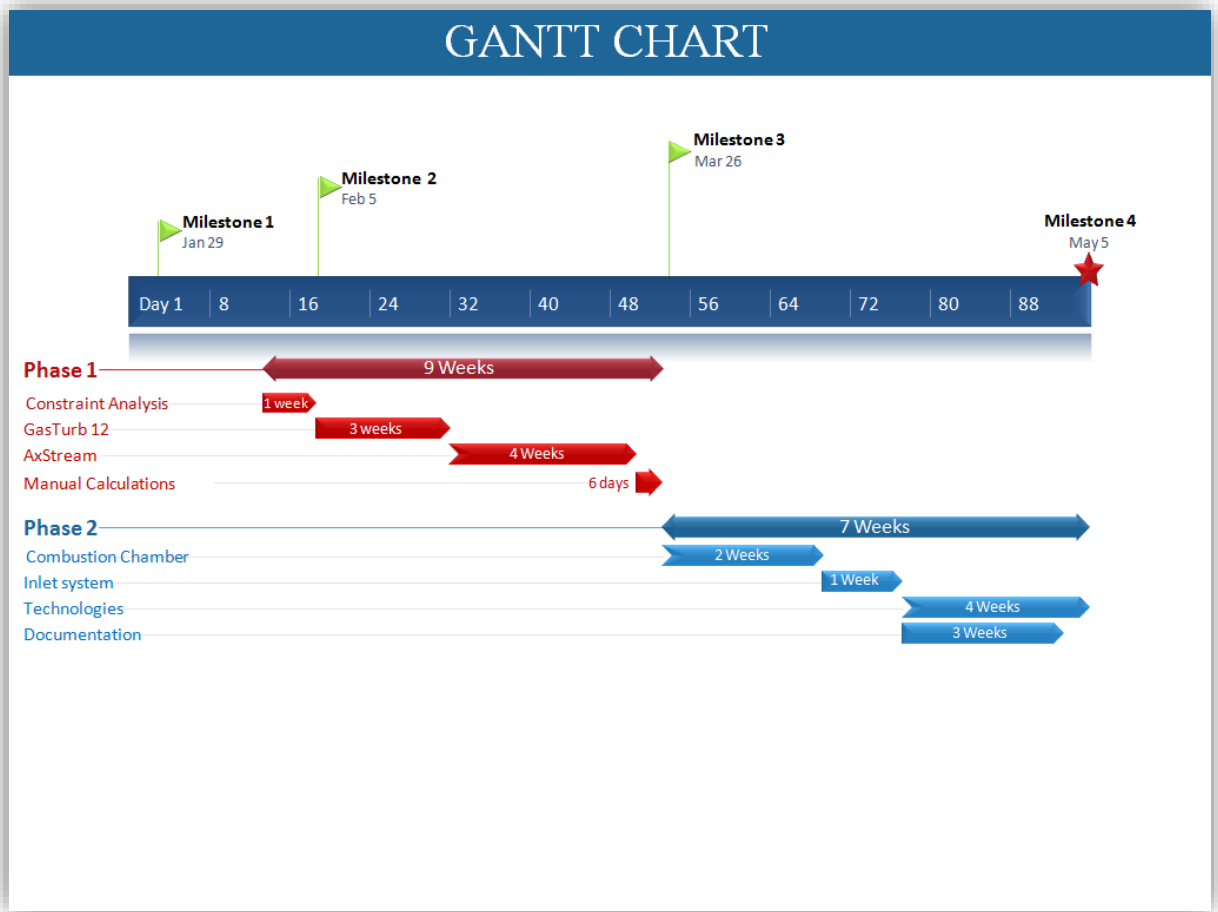

APPENDIX B - Impractical optimized engine cycle

```
           W         T         P        WRstd
Station  lb/s        R       psia       lb/s       FN        =    5315.73 lb
 amb               518.67   14.696
  1      10.580    518.67   14.696                 TSFC      =     0.1199 lb/(lb*h)
  2      10.580    518.67   14.696     10.580      V0        =       0.00 ft/s
 24      10.580    953.11  101.968      2.067      P25/P24   =    1.00000
 25      10.580    953.11  101.968      2.067      P3/P2     =      34.83
  3      10.580   1541.74  511.921      0.524      FN res    =     219.57 lb
 31       9.839    856.52  511.921                 Heat Rate=     7170.1 BTU/(hp*h)
  4      10.016   2636.48  478.646      0.693      WF        =    0.17706 lb/s
 41      10.016   2636.48  478.646      0.693      Loading   =     100.00 %
 43      10.016   1696.84   61.296                 s NOx     =     1.4101
 44      10.016   1696.84   61.296                 Therm Eff=    0.35525
 45      10.016   1696.84   60.990      4.365      P45/P44   =    0.99500
 49      10.016   1266.79   16.945                 P6/P5     =    0.98000
  5      10.016   1266.79   16.945     13.576
  6      10.016   1266.79   16.606                 A8        =      61.67 in²
  8      10.016   1266.79   16.606     13.853      P8/Pamb   =    1.13000
Bleed     0.741   1541.74  511.921                 WBld/W2   =    0.07000
-------------------------------------------        P2/P1     =    1.00000
Efficiencies:     isentr  polytr    RNI    P/P
 Booster          0.8706  0.9000  1.000  6.939     driven by HPT
 Compressor       0.8774  0.9000  3.360  5.020     WCHN/W25 =    0.00000
 Burner           0.9900                 0.935     WCHR/W25 =    0.00000
 HP Turbine       0.9208  0.9000  4.873  7.809     e444 th   =    0.92080
 LP Turbine       0.9141  0.9000  1.029  3.599     eta t-s   =    0.83694
-------------------------------------------        TRQ       =     100.00 %
HP Spool mech Eff 0.9990  Nom Spd  36830 rpm       WCLN/W25 =    0.00000
PT Spool mech Eff 1.0000  Nom Spd  30000 rpm       WCLR/W25 =    0.00000
-------------------------------------------
                                                   PWSD      =    1649.99 hp
                                                   PWSD,eq   =    1781.98 hp
                                                   SFC,eq    =    0.35771 lb/(hp*h)
-------------------------------------------
hum [%]     war0       FHV      Fuel
   0.0   0.00000   18552.4    Generic
```

The above is an example of the cycle optimized to the maximum limit. However due to physical limitations of material capability and thermodynamic considerations we have used the cycle presented in section 4.

APPENDIX C - Additional Turbomachinery Information

COMPRESSOR	Stage 1 (Axial)			Stage 2 (Axial)			Stage 3 (Axial)			Stage 4 (Axial)			Stage 1 (Centrifugal)		
At Rotor outlet	HUB	MEAN	TIP	HUB	MEAN	TIP	HUB	MEAN	TIP	HUB	MEAN	TIP	HUB	MEAN	TIP
Total to total efficiency	0.921	0.921	0.921	0.899	0.899	0.899	0.905	0.905	0.905	0.904	0.904	0.904	0.818	0.878	0.818
Work coefficient	0.881	0.467	0.289	0.662	0.424	0.295	0.534	0.382	0.286	0.443	0.339	0.268	0.769	0.763	0.769
Metal angle (tan.deg.)	61.56	49.14	46.749	56.683	48.521	45.64	54.742	48.916	46.169	54.131	49.715	47.192	NA-	NA-	NA-
Stagger angle (deg.)	44.969	49.349	56.082	46.206	49.362	54.545	47.748	50.135	54.271	48.56	50.455	53.865	NA-	NA-	NA-
Kinematics															
Absolute velocity (ft/s)	830.57	702.96	640.19	769.996	700.575	659.722	742.956	702.313	675.581	732.863	708.148	690.689	1475.803	1475.803	1475.803
Radial velocity	182.72	0	-221.619	148.032	0	-172.754	122.366	0	-139.052	102.008	0	-113.494	636.762	636.762	636.762
Tangential velocity	645.07	469.869	369.505	533.319	427.003	356.034	454.204	384.12	332.788	389.975	341.274	303.386	1331.365	1331.365	1331.365
Axial velocity	489.86	522.861	473.569	535.312	555.402	527.853	575.072	587.946	571.267	612.048	620.49	610.02	-0.341	-0.341	-0.341
Meridional velocity	522.861	522.861	522.861	555.402	555.402	555.402	587.946	587.946	587.946	620.49	620.49	620.49	636.762	636.762	636.762
Thermodynamics															
Total pressure	23.205	23.205	23.205	32.757	32.757	32.757	43.429	43.429	43.429	54.659	54.659	54.659	189.396	189.396	189.396
Total enthalpy (Btu/lb)	143.53	143.53	143.53	160.682	160.682	160.682	176.113	176.113	176.113	189.82	189.82	189.82	282.547	282.547	282.547
Total temperature (deg. R)	597.201	597.201	597.201	668.568	668.568	668.568	732.771	732.771	732.771	789.81	789.81	789.81	1175.623	1175.623	1175.623

TURBINES	Stage 1 (HPT)			Stage 1 (LPT)			Stage 2 (LPT)		
At Rotor outlet	HUB	MEAN	TIP	HUB	MEAN	TIP	HUB	MEAN	TIP
Total to total efficiency	0.906	0.906	0.906	0.918	0.918	0.918	0.93	0.93	0.93
Work coefficient	1.433	1.187	1	0.678	0.532	0.429	1.192	0.749	0.514
Metal angle (tan.deg.)	13.96	13.442	12.903	28.573	25.071	22.346	30.821	23.188	18.668
Stagger angle (deg.)	61.743	68.592	73.73	53.138	62.091	67.653	22.858	55.598	71.161
Isentropic velocity ratio	0.527	0.582	0.636	0.757	0.856	0.954	0.591	0.748	0.905
Zweifel Coefficient	0.694	0.884	1.123	0.74	0.753	0.755	0.76	0.758	0.9
Kinematics									
Absolute velocity (ft/s)	969.672	919.131	878.597	647.383	642.698	639.355	613.556	592.632	581.222
Radial velocity	0	0	0	0	0	0	0	0	0
Tangential velocity	-746.313	-679.353	-623.419	167.662	148.545	133.341	260.561	206.528	171.056
Axial velocity	619.09	619.097	619.097	625.296	625.296	625.296	555.481	555.481	555.481
Meridional velocity	619.09	619.097	619.097	625.296	625.296	625.296	555.481	555.481	555.481
Actual flow angle	14.878	14.354	13.809	28.956	25.3	22.479	31.902	23.81	19.097
Circumferential velocity	1593.169	1750.2	1907.23	1315.793	1485.125	1654.458	1191.613	1503.367	1815.121
Relative velocity	2420.013	2507.192	2605.277	1307.364	1475.616	1644.624	1084.166	1410.798	1735.37
Thermodynamics									
Total pressure	50.919	50.919	50.919	33.44	33.44	33.44	16.945	16.945	16.945
Total enthalpy (Btu/lb)	445.515	445.515	445.515	416.883	416.883	416.883	349.235	349.235	349.235
Total temperature (deg. R)	1853.699	1853.699	1853.699	1734.567	1734.567	1734.567	1453.09	1453.09	1453.09

APPENDIX D - Axial Compressor 1st Stage Velocity Triangles (SI Units)

$$U = 2\pi r_m N = 2\pi(0.0794)\left(\frac{36830}{60}\right) = 306.23\ m/s$$

$$C_a = 154.44\ m/s$$

$$\tan\beta_1 = \frac{U}{C_a} = \frac{306.23}{154.44} = 1.982$$

$$\beta_1 = 63.237°$$

$$V_1 = \frac{C_a}{\cos\beta_1} = \frac{154.44}{\cos 63.237°} = 343\ m/s$$

De Haller factor for stage I

$$\frac{V_2}{V_1} = 0.72$$

$$V_2 = 0.72(342) = 246.96\ m/s$$

$$\Delta T_0 = \frac{438.672 - 288}{4} = 37.668\ K$$

$$C_{w_2} - C_{w_1} = \frac{C_p \Delta T_0}{\lambda U} = \frac{1.005\times10^3 \times 37.668}{0.98 \times 306.232} = 126.142\ m/s$$

$$C_{w_1} = 0$$

$$C_{w_2} = 126.142\ m/s$$

$$\tan\alpha_2 = \frac{C_{w_2}}{C_a} = 0.81677$$

$$\alpha_2 = 39.24°$$

$$\tan\beta_2 = \frac{U - C_{w_2}}{C_a} = \frac{306.232 - 126.142}{154.44} = 1.166$$

$$\beta_2 = 49.384°$$

$$C_1 = C_a \cos 0 = 154.44\ m/s$$

$$C_2 = C_a \cos 39.24° = 119.61\ m/s$$

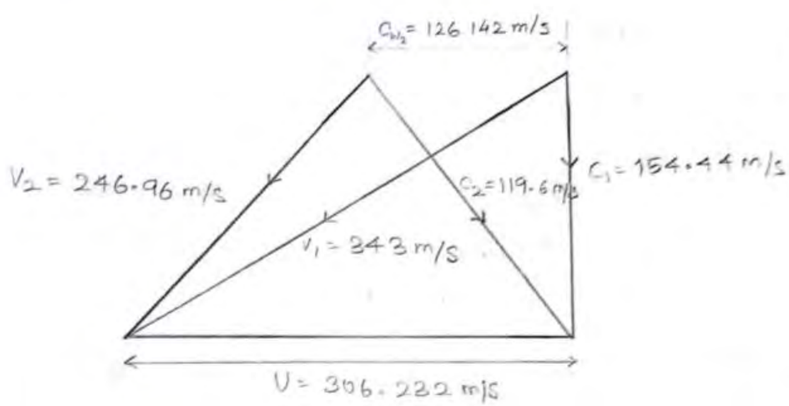

APPENDIX E - HPT 1st Stage Velocity Triangles (SI Units)

$r_m = 13.895\,cm$ $\quad T = 1365.68\,K$ $\quad P = 11\,bar$ $\quad \eta = 0.9$ $\quad m = 4.55\,kg/s$

$\Delta T = 293.58\,K$

$$U = 2\pi r_m N = 2\pi(0.13895)\left(\frac{36830}{60}\right) = 536\,m/s$$

$$\Psi = \frac{2c_p\Delta T}{U^2} = \frac{2\times 1.148\times 293.58\times 10^3}{(536)^2} = 2.34622$$

Assume $\phi = 0.8$ and $\alpha_3 = 10^\circ$

$$\tan\alpha_3 = \tan\beta_3 + \frac{1}{\phi}$$

$$\tan\beta_3 = \tan 10^\circ + \frac{1}{0.8} = 1.426$$

$$\beta_3 = 55^\circ$$

$$\tan\beta_3 = \frac{1}{2\phi}\left(\frac{1}{2}\Psi + 2\Lambda\right)$$

$$1.426 = \left(\frac{1}{2(0.8)}\left(\frac{1}{2}(2.34622) + 2\Lambda\right)\right)$$

$$\Lambda = 0.5545$$

$$\tan\beta_2 = \frac{1}{2\phi}\left(\frac{1}{2}\Psi - 2\Lambda\right)$$

$$\tan\beta_2 = \frac{1}{2(0.8)}\left(\frac{1}{2}(2.34622) - 2(0.5545)\right)$$

$$\beta_2 = 2.3^\circ$$

$$\tan\alpha_2 = \tan\beta_2 + \frac{1}{\phi} = 0.04 + 1.25 = 1.29$$

$$\alpha_2 = 52.2^\circ$$

$$Ca_2 = U\phi = 536(0.8) = 428.8\,m/s$$

$$c_2 = \frac{Ca_2}{\cos\alpha_2} = \frac{428.8}{\cos(52.2)} = 699.6\,m/s$$

Assume $Ca_2 = Ca_3$ and $c_1 = c_3$

$$C_3 = \frac{Ca_3}{\cos\alpha_3} = \frac{428.8}{\cos 10^\circ} = 435.4\,m/s$$

$$V_2 = \frac{Ca_2}{\cos\beta_2} = \frac{428.8}{\cos(2.3^\circ)} = 429.1\,m/s$$

$$V_3 = \frac{Ca_3}{\cos\beta_3} = \frac{428.8}{\cos(55^\circ)} = 747.6\,m/s$$